land

MDPI

Article

Spatial Distribution and Driving Mechanisms of Soil Organic Carbon in the Yellow River Source Region

Zhenying Zhou [1,2], Jinxi Su [1,2], Haili Ma [1,2], Xinyu Wang [1,2] and Huilong Lin [1,2,*]

[1] State Key Laboratory of Herbage Improvement and Grassland Agro-Ecosystems, College of Pastoral Agriculture Science and Technology, Lanzhou University, Lanzhou 730020, China; 120220900640@lzu.edu.cn (Z.Z.); sujx2023@lzu.edu.cn (J.S.)
[2] Key Laboratory of Grassland Livestock Industry Innovation, College of Pastoral Agriculture Science and Technology, Lanzhou University, Lanzhou 730020, China
* Correspondence: linhuilong@lzu.edu.cn

Abstract

Soil organic carbon (SOC) plays a vital role in regional carbon cycling and ecosystem services. However, previous studies have primarily focused on spatial patterns and environmental drivers, with limited attention to long-term observations, underlying mechanisms, and large-scale modeling. In this study, we collected surface soil samples (0–20 cm) and integrated topography, soil physicochemical properties, climate, vegetation, and MODIS remote sensing data to develop 16 SOC prediction models using linear regression and machine learning approaches. SOC was significantly correlated with latitude, mean annual temperature, and precipitation and negatively associated with several remote sensing indices. The LASSO-selected variable set combined with a support vector machine (SVM) achieved the highest predictive accuracy (R^2 = 0.53, RMSE = 36.19). From 2001 to 2020, the mean SOC stock in the Yellow River source region was estimated at 1683.98 g C/m^2, showing higher values in the southeast and lower values in the northwest. Alpine meadow exhibited the highest total stock due to its extensive coverage, whereas the cold temperate wet coniferous forest had higher mean content and unit area value, indicating strong carbon sequestration potential. This study identifies key SOC drivers and mechanisms, provides quantitative estimates of regional SOC content and stock, and offers a scientific basis for grassland carbon management and large-scale digital soil mapping.

Keywords: soil organic carbon; driving mechanisms; grassland ecosystem; carbon sink

Check for updates

Academic Editor: Amrakh I. Mamedov

Received: 22 October 2025
Revised: 22 December 2025
Accepted: 25 December 2025
Published: 29 December 2025

Copyright: © 2025 by the authors. Licensee MDPI, Basel, Switzerland. This article is an open access article distributed under the terms and conditions of the Creative Commons Attribution (CC BY) license.

1. Introduction

1.1. Motivation

Grassland ecosystems, one of the dominant terrestrial ecosystem types, cover approximately 40% of the global land surface [1,2] and provide essential ecosystem services, including carbon sequestration, climate regulation, water conservation, soil retention, biodiversity maintenance, and livestock production. Globally, grasslands store an estimated 761 Gt of carbon, of which 89.4% is retained in soils [3]. They sequester nearly 10^{12} kg of greenhouse gases annually [4], and even minor changes in soil carbon stocks can markedly influence atmospheric CO_2 concentrations, thereby affecting global climate through the greenhouse effect [5–7]. Consequently, grassland ecosystems play a pivotal role in the global carbon cycle and climate regulation.

China possesses extensive grassland resources, and the Source Region of the Yellow River (SRYR)—dominated by alpine grasslands—serves as a key ecological barrier on

the Qinghai–Tibet Plateau, with substantial soil carbon stocks [8–10]. However, intensified climate warming has heightened ecological vulnerability in the region. Large-scale degradation of alpine grasslands, manifested by the emergence of "black soil patches," has severely disrupted ecosystem functions and threatened the stability of regional grassland carbon pools. Therefore, assessing the stock, spatial distribution, and temporal variability of soil organic carbon (SOC) in the SRYR—especially through dynamic monitoring and quantitative evaluation—is crucial for ecological conservation, carbon sink management, and climate change mitigation.

Nonetheless, accurate digital mapping of SOC in the SRYR is challenged by substantial environmental heterogeneity. The region features highly complex topography, characterized by pronounced elevation gradients and steep slopes [11,12], resulting in strong spatial variability in SOC distribution. In addition, harsh climatic conditions—such as low temperatures, recurrent freeze–thaw cycles, and uneven precipitation—significantly influence SOC decomposition and stabilization across seasons, further complicating SOC modeling and increasing the uncertainty of spatial prediction [13–15].

1.2. Related Work

1.2.1. Model Simulation and Digital Mapping of SOC

With the increasing availability of soil organic carbon (SOC) data, machine learning (ML) has gained considerable attention for its superior performance in SOC stock simulations [16–18]. A range of models—including Boosted Regression Trees (BRT), Random Forests (RF), Cubist, support vector machines (SVM), and Kriging—have been extensively employed in digital mapping of SOC spatial distribution [17,19–21], substantially improving prediction accuracy. For example, Ballabio et al. (2014) applied an SVM model to estimate SOC stocks in Cyprus, achieving a high predictive performance with an R^2 of 0.81 [22]. Ye et al. (2021) reported that the Light Gradient Boosting Machine (LGBM) outperformed RF in both accuracy and computational efficiency [23]. Similarly, Tziachris et al. (2019) demonstrated that ML models (RF and GB) achieved higher precision than geostatistical approaches or multivariate regression models when predicting soil organic matter in the Kastoria region [24].

A variety of SOC models have been developed based on remote sensing-derived correlations or process-based mechanisms [25–27]. However, most existing models exhibit strong regional specificity due to differences in model development environments [28–32], limiting their applicability to SOC stock estimation in the alpine grasslands of the Source Region of the Yellow River (SRYR). This underscores the need to develop region-specific models tailored to the unique environmental conditions of the SRYR.

Current research on SOC commonly relies on soil sampling conducted at multiple spatial scales—global, national, and regional—using datasets collected across diverse geographic settings [33–36]. These datasets are integrated with remote sensing products to improve the spatial characterization of SOC [37–42].

However, as noted by Siewert, a major constraint to accurate SOC mapping remains the scarcity of high-quality soil data [43]. In regions characterized by complex topography, high elevation, and limited accessibility, such as alpine and mountainous environments, SOC mapping must also contend with substantial data collection costs and logistical challenges [36,44].

1.2.2. Spatiotemporal Distribution of SOC

Existing research has largely concentrated on the static spatial distribution of soil organic carbon (SOC) [45,46]. However, SOC is not constant: its spatiotemporal patterns are continuously adjusted under the influence of climate change, land use transitions,

vegetation cover dynamics, and human activities [34]. This variability becomes more complex in regions featuring heterogeneous ecological environments, highly variable climatic conditions, and anthropogenic disturbances [47–49]. For instance, grazing activities exert profound effects on SOC accumulation and loss across different soil depths [50–52]. Therefore, investigating the spatiotemporal distribution of SOC in the Source Region of the Yellow River (SRYR) is crucial for revealing its dynamic changes and for providing accurate support for ecological protection, land use planning, and carbon management.

1.2.3. Driving Factors of Soil Organic Carbon

Extensive research has been conducted globally on the driving factors of soil organic carbon (SOC), with most studies focusing on climate, topography, vegetation type, and land use. Climate factors, particularly temperature and precipitation, have been shown to exert significant positive effects on SOC stock [53–55]. Topographic variables, such as slope and elevation, are also recognized as major controls of SOC distribution [56,57]. For instance, Meng Zhu et al. reported that elevation zones and slope positions influence SOC distribution in semi-arid alpine grasslands of northwestern China [44].

SOC accumulation is additionally closely associated with soil moisture conditions [58–60]. While many studies have explored the effects of individual factors such as climate or topography, others have examined the impacts of human activities and land use change on SOC [61–63]. However, most existing studies still lack a comprehensive assessment of the combined effects of multiple factors on SOC dynamics. For example, Jitendra Ahirwal et al. found no significant correlations between environmental variables (elevation, latitude, precipitation, and temperature) and carbon stocks in the Indian Himalayan region [64]. Similarly, Nikou Hamzehpour et al. reported that in the western part of Urmia Lake, Iran, enhanced vegetation index (EVI) and sand content had stronger influences on SOC variation than slope and land cover type, and significant interactions were detected between EVI–moisture–SOC and EVI–sand–SOC [65]. These findings suggest that in regions with complex terrain, soil properties may interact with climatic and topographic factors to influence SOC distribution [66,67]. Consequently, the applicability of these driving mechanism studies remains to be validated in the Source Region of the Yellow River (SRYR).

1.2.4. Research Aim

As a critical carbon pool in terrestrial ecosystems, grassland soil organic carbon (SOC) plays a key role in climate regulation and ecological security. However, for the Source Region of the Yellow River (SRYR), fine-scale mapping, mechanistic analysis, and value assessment of SOC based on long-term monitoring and high-density datasets remain limited. This study aims to develop an optimal SOC modeling framework for the SRYR, elucidate its spatiotemporal distribution and driving mechanisms, and assess its carbon sink's ecological and economic value. The specific objectives are as follows:

1. To construct an optimal SOC prediction model for the SRYR based on multi-source environmental data and machine learning approaches, accurately capturing the spatial distribution of the 0–20 cm soil layer;
2. To systematically analyze the spatiotemporal dynamics of SOC using the optimal model, identify key driving factors, and clarify their underlying mechanisms;
3. To quantitatively evaluate the carbon sequestration function of SOC based on its spatiotemporal dynamics and estimate the associated ecological and economic values.

2. Materials and Methods

2.1. Study Area

The Source Region of the Yellow River (SRYR) (Figure 1) is located between 95.54°–103.24° E and 32.12°–36.36° N, covering an area of approximately 1.32×10^5 km^2. The terrain generally declines from west to east, with elevations ranging from 2513 to 6248 m [68]. The climate is classified as sub-frigid semi-humid plateau, exhibiting typical high altitude continental characteristics [69]. The region experiences strong solar radiation, with an annual sunshine duration of 2000–3000 h. Precipitation is concentrated from June to September, with an annual mean of approximately 500 mm [70]. The SRYR is characterized by arid and cold conditions, with widespread soil desiccation and hypoxia. Soils are predominantly alpine meadow soils [71,72]. The study area has a low population density, and the local economy relies primarily on grassland animal husbandry [73]. Increasing human activity has caused significant ecosystem degradation, making ecological protection and restoration urgent. According to Ren [74], the Comprehensive and Sequential Classification System (CSCS) categorizes natural and artificial grasslands by quantifying indicators such as annual accumulated temperature and humidity indices combined with vegetation characteristics, thereby revealing zonal and ecological patterns of grasslands. Based on this classification, the SRYR is dominated by alpine meadow type grasslands.

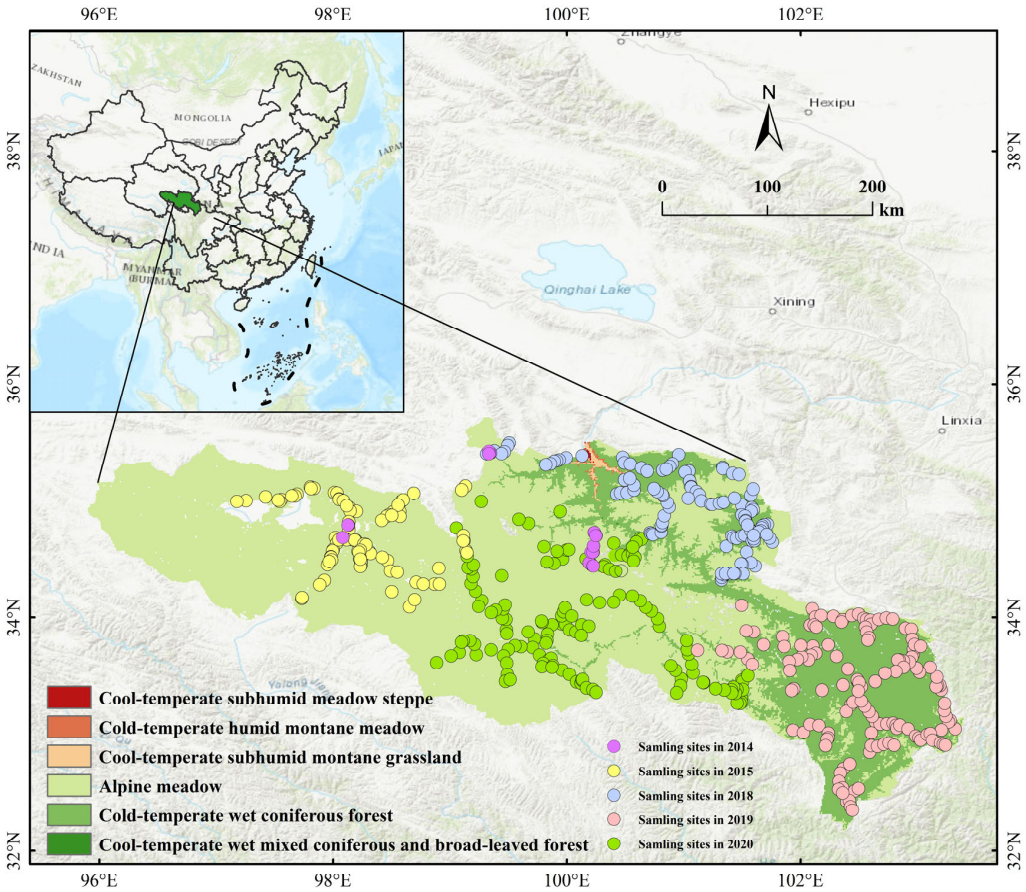


Figure 1. The layout of land cover types and sampling sites from 2001 to 2020 across the SRYR. Note: Generated based on the Comprehensive Sequential Classification System (CSCS) and validated through field investigations.

2.2. Data Resource

2.2.1. Measured SOC Data and Processing

Constructing a reliable measured dataset is a critical foundation for SOC modeling, and systematic sampling in the Source Region of the Yellow River (SRYR) is essential [75]. Conditional Latin Hypercube Sampling (cLHS) [76] is particularly suitable for applications such as digital soil mapping, as it significantly improves the reliability of soil property predictions compared with simple random sampling, especially under limited resources [77]. Sampling points were established using the clhs package in R (version 4.5.0) via RStudio, incorporating terrain, climate, soil physicochemical properties, vegetation factors, and remote sensing indices, with a "cost layer" applied to constrain point locations and distributions, thereby ensuring representative coverage while minimizing sampling costs. A total of 619 spatially representative points were established, and at each point, three soil cores (0–20 cm) were randomly collected and combined into a composite sample. The samples were air-dried in the laboratory, debris removed, and ground through a 0.25 mm sieve for subsequent analysis. Soil organic carbon (SOC) stock was determined using the potassium dichromate oxidation method with external heating [78,79].

2.2.2. Environmental Variables

This study collected environmental variables from multiple sources, including terrain factors, climatic factors, soil physicochemical properties, vegetation factors, and remote sensing indices. Daily maximum and minimum temperatures and precipitation data for 2014–2020 were obtained from 14 meteorological stations in the Source Region of the Yellow River (SRYR) via the China Meteorological Data Service Center (https://data.cma.cn/). Annual mean temperature, annual precipitation, and growing degree days ≥ 0 °C were derived using the ANUSPLIN spatial interpolation method.

MODIS (Moderate-resolution Imaging Spectroradiometer) products were downloaded from Google Earth Engine (https://earthengine.google.com/), primarily including various vegetation indices (e.g., NDVI, EVI, SAVI, MSAVI, NDWI) and relevant spectral bands (visible, NIR, and MIR) to characterize vegetation growth and ecological conditions. Summer (July–September) and winter (October–December) were selected as study periods, and all MODIS images were resampled to 500 m. Vegetation indices are widely applied in remote sensing to reflect vegetation cover and growth vigor [80–82], with calculation methods of relevant indices shown in Table A1.

Soil property data were obtained from the Cold and Arid Regions Science Data Center [83], including surface layer (0–30 cm) sand (sand1) and clay (clay1) and subsurface layer (30–100 cm) sand (sand2) and clay (clay2). Volumetric rock fragment content (>2 mm) was obtained from the China Dataset of Soil Properties for Land Surface Modeling [84] (https://cstr.cn/18406.11.Terre.tpdc.301235). Soil pH and bulk density (BD) were retrieved from the global SoilGrids database (https://soilgrids.org/) at 250 m spatial resolution. These soil properties are regarded as representative of the long-term pedogenic background of different grassland types and are relatively stable compared to climatic variables. Agricultural, forestry, animal husbandry, and fishery production data (in CNY 100 million) were sourced from the 2020 Statistical Yearbooks of Qinghai and Sichuan provinces.

In summary, multi-source data, including meteorological, remote sensing, soil, and statistical datasets, were integrated, and after preprocessing, a total of 81 input variables were constructed for SOC prediction modeling. The selected variables cover the five categories mentioned above, with the complete list provided in Table A2.

2.3. Methods

The methodological framework and analytical workflow are presented in Figure 2.

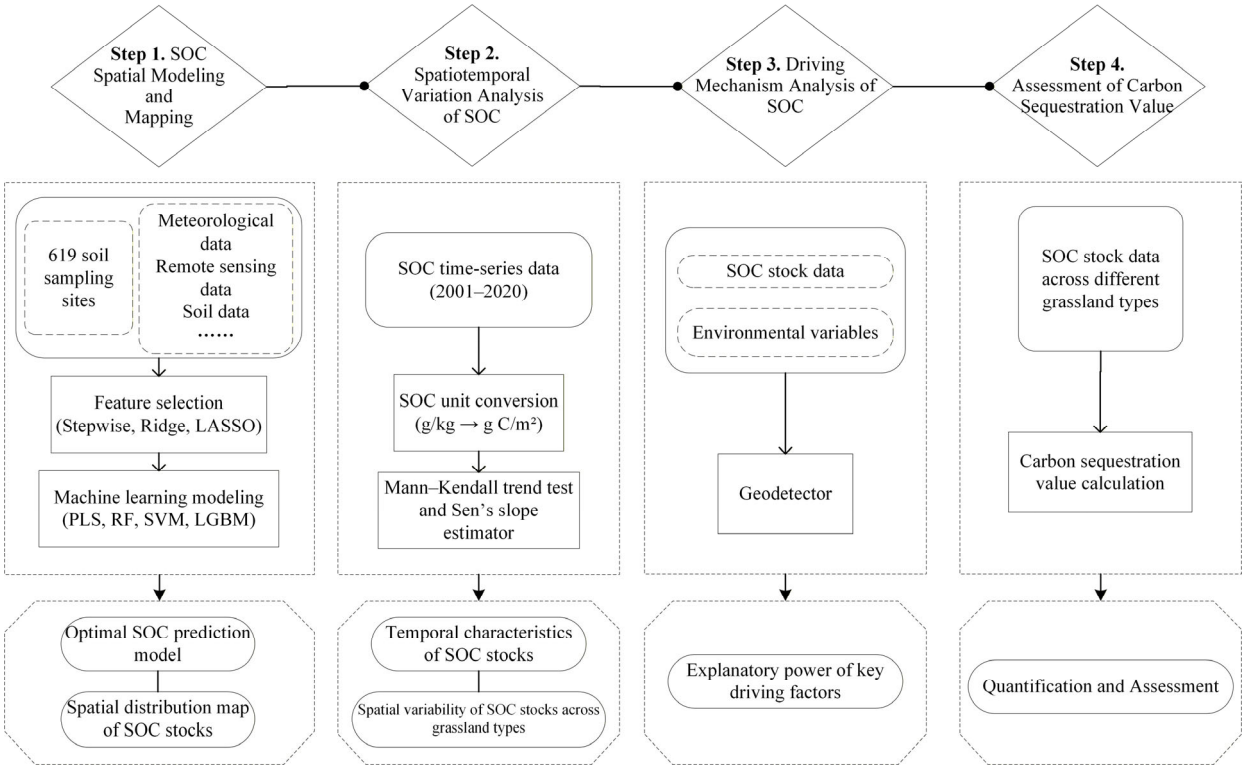


Figure 2. Methodological framework and analytical workflow.

2.3.1. Variable Selection

A total of 81 variables were selected as input predictors for SOC modeling, covering topographic, climatic, soil physicochemical, vegetation, and remote sensing factors. Due to strong correlations and multicollinearity among SOC-related variables, variable selection is essential to prevent model overfitting and improve computational efficiency.

Stepwise regression iteratively introduces or removes variables based on statistical significance, retaining key predictors while eliminating redundant factors to enhance model fit [85,86]. Ridge regression incorporates a penalty term into ordinary least squares, effectively mitigating multicollinearity, stabilizing regression coefficients, and excluding unstable variables [87,88]. The LASSO method applies a shrinkage penalty to achieve variable compression and automatic selection, combining the advantages of ridge regression and subset selection, and is particularly suited to high-dimensional data [89,90]. All variable selection procedures were implemented in SPSS 19.0 and MATLAB 2019b to optimize the predictive performance of the SOC model.

2.3.2. Machine Learning Methods

Based on the systematically sampled SOC database and the refined variable set obtained through multiple selection techniques, four machine learning predictive models were developed to simulate SOC stock in the Source Region of the Yellow River: Partial Least Squares Regression (PLS), Random Forest (RF), support vector machine (SVM), and the improved gradient boosting algorithm LightGBM (LGBM). To ensure model generalization and robustness, all 619 samples were randomly divided into a training set (70%, 429 samples) and a testing set (30%, 190 samples). During model training, hyperparameters were optimized using ten-fold cross-validation combined with Bayesian search. After determining the optimal parameter configuration, each model was applied to the testing set for prediction, and model performance was evaluated using the coefficient of determination (R^2) and root mean square error (RMSE).

Partial Least Squares (PLS) regression combines principal component analysis with regression by extracting latent components that capture the covariance structure between predictors and the response variable. It effectively addresses multicollinearity and small-sample limitations while integrating the strengths of multiple linear regression, canonical correlation, and principal component analysis [91,92]. In this study, PLS modeling was implemented using the plsr() function in R Studio, and the optimal number of latent components was determined based on the minimum root mean square error (RMSE) during model calibration.

Random Forest (RF), an ensemble learning method based on decision trees, constructs multiple trees through bootstrap sampling and aggregates predictions via voting or averaging. It is highly robust for data imbalances and variable importance heterogeneity, offering strong predictive performance with a low risk of overfitting [93,94]. In this study, RF modeling was implemented using the randomForest package in R Studio, with ntree = 1000 and mtry set to one-third of the total input variables to balance model accuracy and diversity.

Support vector machine (SVM), grounded in Vapnik–Chervonenkis (VC) theory and structural risk minimization, is capable of handling both linear and nonlinear relationships while maintaining strong generalization performance under limited sample sizes [95,96]. The SVM regression model was developed using the e1071 package in R Studio with a radial basis function (RBF) kernel, and key parameters (gamma and cost) were tuned using the tune() and svm() functions.

LightGBM, an enhanced gradient boosting decision tree (GBDT) algorithm, incorporates histogram-based optimization, leaf-wise growth, Gradient-based One-Side Sampling (GOSS), and Exclusive Feature Bundling (EFB), thereby improving computational efficiency while retaining high accuracy, particularly for large-scale datasets [97]. Model development was conducted in Python (version 3.8.20) using the LightGBM library, with key parameters configured as num_leaves = 20, max_depth = 5, bagging_fraction = 0.8, feature_fraction = 0.95, and learning_rate = 0.2.

2.3.3. SOC Unit Conversion

Soil samples were oxidized with a standardized mixture of $K_2Cr_2O_7$ and concentrated H_2SO_4 in a temperature-controlled oil bath. Following digestion, the residual $K_2Cr_2O_7$ was back-titrated against a $FeSO_4 \cdot 7H_2O$ standard solution using o-phenanthroline as a redox indicator. The SOC mass was determined based on the volumetric consumption of the oxidant.

For analytical consistency and spatial comparability, the SOC concentrations (measured in g/kg) were converted to areal SOC stocks (g C/m^2) by incorporating soil bulk density and the volumetric fraction of coarse fragments. The conversion was performed using the following equation:

$$SOC_{stock}\left(\mathrm{g\,C/m^2}\right) = SOC\,(\mathrm{g/kg}) \times BD\left(\mathrm{kg/m^3}\right) \times Z\,(\mathrm{m}) \times (1 - Rock_{vol}) \quad (1)$$

where BD is the bulk density of the soil layer (kg/m^3), Z is the thickness of the sampled soil layer (m), and $Rock_{vol}$ is the volumetric fraction of coarse fragments (>2 mm).

2.3.4. Spatiotemporal Analysis of SOC

To characterize the temporal and spatial variations of soil organic carbon (SOC) across the study area, the Mann–Kendall (MK) trend test was combined with Sen's slope estimator. The MK test is a rank-based nonparametric method [98,99] that does not require assumptions about data distribution. It is robust to non-normality, missing values, and outliers, making it suitable for detecting long-term trends in ecological and hydrological

time series. Sen's slope was used to quantify the magnitude of the trend, representing the average rate of change per unit time.

Mann–Kendall Trend Test and Sen's Slope Estimation

Using annual SOC stock concentration (g C/m^2) for the period 2001–2020, a time series was constructed and analyzed with the pymannkendall package in Python to determine whether a significant monotonic trend exists. The MK test statistic is defined as follows:

$$S = \sum_{i=1}^{n-1} \sum_{j=i+1}^{n} sgn(x_j - x_i) \quad (2)$$

where x_i and x_j are the observed values at times i and j and sgn ( ) is the sign function. A predominance of later values exceeding earlier ones yields $S > 0$, indicating an increasing trend; $S < 0$ implies a decreasing trend. Trend significance was assessed using the p value returned by the library function, with a significance level of $\alpha = 0.05$.

Sen's slope was calculated as follows:

$$Q = median\left(\frac{x_j - x_i}{j - i}\right), i < j \quad (3)$$

The parameter Q represents the average rate of change in SOC stock over time (g C/m^2/year), where positive values indicate an increasing trend and negative values indicate a decline. Based on the results of the MK test and Sen's slope estimation, the spatial distribution of SOC trends across the study area was derived, and the proportion of significant trends as well as the mean rate of change were further summarized within different grassland types.

Geographical Detector

Geodetector is a statistical tool designed to analyze spatial stratified heterogeneity and identify its driving factors [100]. The underlying principle is that if the spatial distribution of an explanatory factor aligns with that of the dependent variable, the factor is likely a driver of the variable's spatial heterogeneity. Geodetector comprises four components: the factor detector, which quantifies the explanatory power of each factor; the risk detector, which identifies differences between strata; the interaction detector, which evaluates the interaction effects between factors; and the ecological detector, which compares their relative importance.

In this study, a 1 km × 1 km fishnet grid was constructed in ArcGIS Pro (version 3.4.2), and SOC data were aggregated with the common factors retained across the three variable selection methods. The factor detector was first employed to calculate the explanatory power of each factor, followed by the risk detector to identify high- and low-risk strata. The interaction detector was then used to determine interaction types, and the ecological detector to compare differences in explanatory strength. The results included rankings of factor explanatory power, stratified statistics, interaction patterns, and relative strengths, which were visualized through charts to reveal the driving mechanisms of SOC spatial distribution in the headwaters of the Yellow River.

3. Results

3.1. SOC Estimation Model Performance and Comparison

3.1.1. Correlation and Regression Analysis

SOC showed significant correlations with multiple environmental factors. Topographically, SOC was positively correlated with longitude (r = 0.231) and negatively with latitude

($r = -0.357$; $p < 0.01$). Among soil properties, SOC was positively correlated with clay content (clay1, clay2; $r = 0.126$–0.177, $p < 0.01$). Meteorologically, SOC was negatively correlated with accumulated temperature ($r = -0.294$) and winter nighttime soil temperature (LsTN–W; $r = -0.271$) but positively correlated with annual precipitation ($r = 0.222$; all $p < 0.01$). SOC also exhibited significant correlations with 26 vegetation factors and 24 remote sensing indices. Vegetation indices such as NDVI, NDVGI, OSAVI, TVI, and SAVI showed coefficients mostly between 0.10 and 0.19, with NDVGI–W ($r = 0.189$) and TVI–W ($r = 0.167$) being the highest. Vegetation indices showed inconsistent patterns across different seasons. Summer indices were mostly positively correlated, while winter indices included both positive (NDVI–W, NDVGI–W) and negative correlations (RVI-W, BI-W, SATVI-W), reflecting seasonal variation in the SOC–vegetation relationship. For remote sensing, SOC was negatively correlated with most winter spectral bands (b1-W to b7-W), particularly b7-W ($r = -0.372$), whereas several summer indices (A-S, B-S, Far-S, Lai-S) were positively correlated. These results indicate that SOC is closely linked to vegetation and responds sensitively to seasonal spectral variations (see Tables A3–A5).

When the stepwise regression (SR), ridge regression (RR), and Least Absolute Shrinkage and Selection Operator (LASSO) methods were applied for variable selection, the variable sets retained 13, 30, and 12 variables, respectively (Table 1). Seven factors—latitude, slope, accumulated temperature, annual precipitation, pH, winter band 7 (b7-W), and B-W were common to all methods. The stepwise regression model additionally included NDSI-S, b2-S, b6-W, MIR-W, A-W, B-W, and E-S and accounted for 44.3% of the variation in SOC samples, with an adjusted R^2 of 0.43, significant according to the F–test. Ridge regression with k set to 0.71 retained 30 variables, including the seven common factors as well as Lon, Alt, E-S, D-W, NDSI-S, b6-S, b7-S, LSTD-S, LSTN-W, and BLUE-W ($p < 0.05$) and accounted for 36.5% of the variation in SOC samples, with an adjusted R^2 of 0.27. LASSO analysis identified 12 variables—Lat, Slope, AT, AP, LsTD-S, clay2, pH, B-W, E-W, D-W, b6-W, and b7-W—that were selected in over 50 iterations, indicating their significant influence on SPYR SOC stock compared with other variables.

Table 1. Main influencing factors of SOC in SPYR.

	Meteorological Factors	Topographic Factor	Soil Factors	Vegetation Indices	Remote Sensing Bands
SR	AT, AP	Lat, Slope	pH	NDSI-S	b2-S, b6-W, b7-W, MIR-W, A-W, B-W, E-S
RR	AT, AP, LsTD-S, LsTN-S, LsTN-W	long, Lat, Alt, Slope	clay1, clay2, sand2, pH	EVI-W, BI-W, NDSI-S, NDWI-W, RVI-W, SCI-W	B-W, E-S, E-W, D-W, b6-S, b7-S, b1-W, b2-W, b4-W, b7-W, BLUE-W
LASSO	AT, AP, LsTD-S	Lat, Slope	clay2, pH		B-W, E-W, D-W, b6-W, b7-W

Note: The meanings of the abbreviations are shown in Table A2.

3.1.2. Model Performance

When comparing different models using the same variable set, SVM and LGBM clearly outperformed PLS and RF (Figure 3). Using the LASSO-selected variables, the SVM model achieved an R^2 of 0.53 and an RMSE of 36.190, while the LGBM model reached an R^2 of 0.51 and an RMSE of 37.768, both significantly better than the PLS model ($R^2 = 0.37$, RMSE = 57.793). Comparisons across variable sets for the same model also revealed performance differences. For LGBM, R^2 varied only by 0.02 across different

variable sets, with RMSE ranging from 36.863 to 39.026. In contrast, SVM performance was more sensitive to variable selection, with R^2 = 0.53 and RMSE = 36.190 under the LASSO set, but was slightly lower under the complete set (CS) (R^2 = 0.43, RMSE = 39.971).

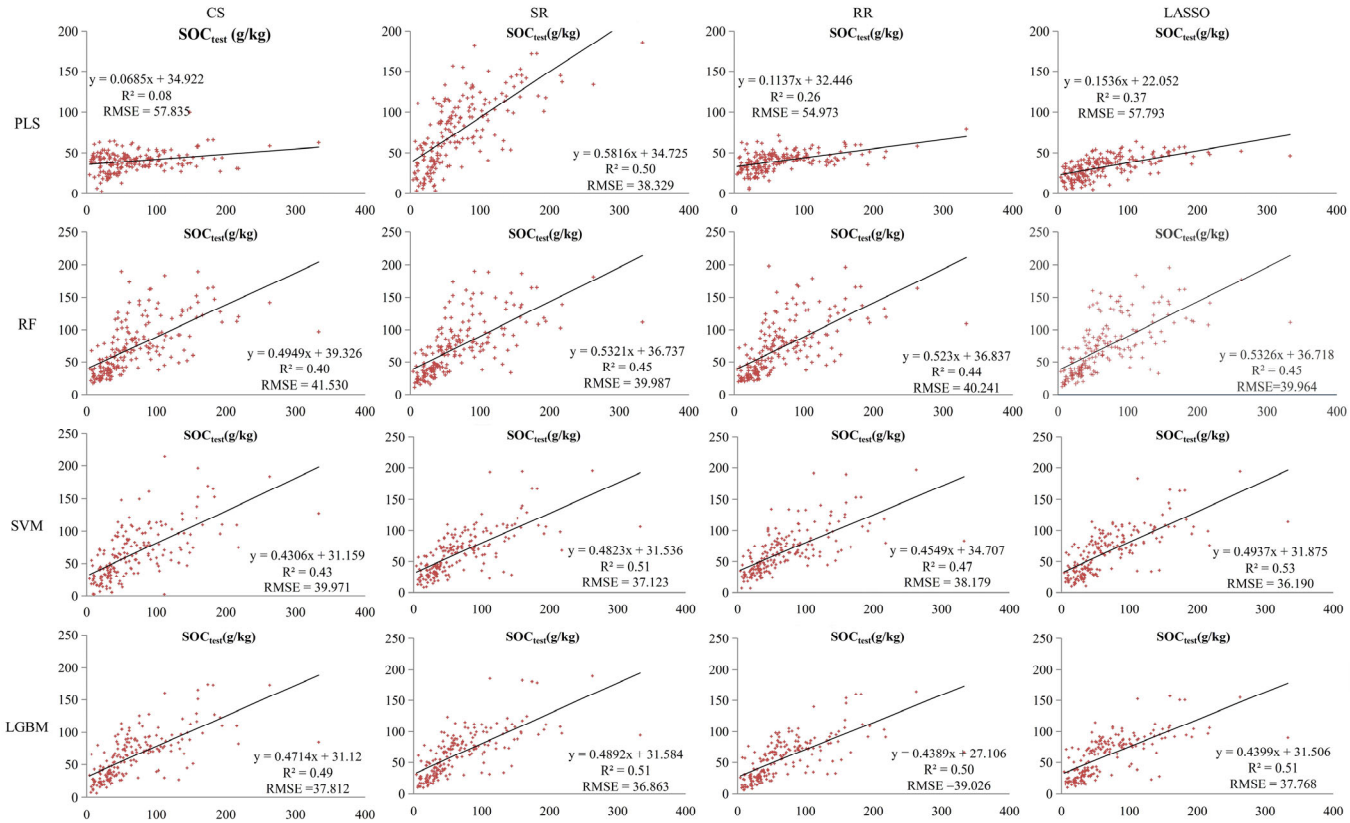


Figure 3. Model performance across 16 machine learning models (test set; X-axis: predicted values; Y-axis: observed values; Unit: g/kg).

Overall, the SVM model combined with the LASSO-selected variables performed best, achieving an R^2 of 0.53 and an RMSE of 36.190, indicating its capability to effectively capture the complex nonlinear responses of SOC stocks to multiple environmental factors and reproduce their spatial variability. The LGBM model showed stable performance, with an R^2 around 0.50 and minimal RMSE variation across variable sets, demonstrating strong generalization ability. Considering both fitting accuracy and prediction error, the SVM–LASSO combination represents the optimal approach, followed by LGBM.

3.2. Spatiotemporal Distribution

3.2.1. Temporal Characteristics Analysis

After performing unit correction by converting SOC concentrations from g/kg to SOC stocks expressed in g C/m^2, Mann–Kendall trend analysis for each year indicated a significant increasing trend in SOC stock from 2001 to 2020 (τ = 0.389, p = 0.018). Sen's slope estimated an average annual increase of 11.69 g C/m^2 in SOC stock (Table 2). During this period, the annual mean SOC stock in the study area ranged from 1486.11 to 1841.27 g C/m^2, showing interannual fluctuations but an overall increasing trend. Quartile ranges remained relatively stable (25%: 958.25–1625.16 g C/m^2; 75%: 1997.55–2238.98 g C/m^2), suggesting that while SOC stock fluctuated over the years, the overall distributional structure remained largely unchanged (Figure 4). The mean and median SOC stock followed very similar trajectories, indicating that the distribution of SOC stock was approximately symmetric.

The standard deviation was approximately 280–670 g C/m^2, suggesting moderate spatial variability while maintaining overall stability.

Table 2. Mann–Kendall test results for SOC stock (2001–2020).

Trend	h	*p* Value	Tau	Sen's Slope
increasing	True	0. 018	0. 389	11.685

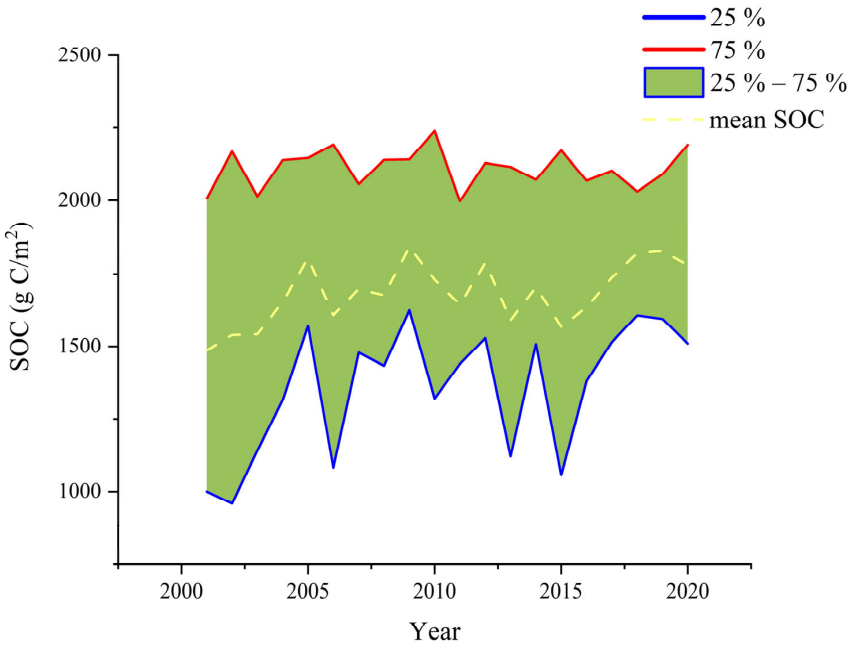


Figure 4. Temporal distribution characteristics of SOC stock from 2001 to 2020 (mean and quartiles).

The results of the 5-year sliding window Mann–Kendall trend analysis applied to SOC data from 2001 to 2020 show that the pattern of SOC stock changes differed across time periods (Figure 5). Among all sliding windows, only the periods 2001–2005 and 2015–2019 passed the significance test (p = 0.027, Tau = 1), showing clear increasing trends. The corresponding Sen's slope values were 68.33 and 75.60, which means that SOC increased at a relatively high rate during these two periods.

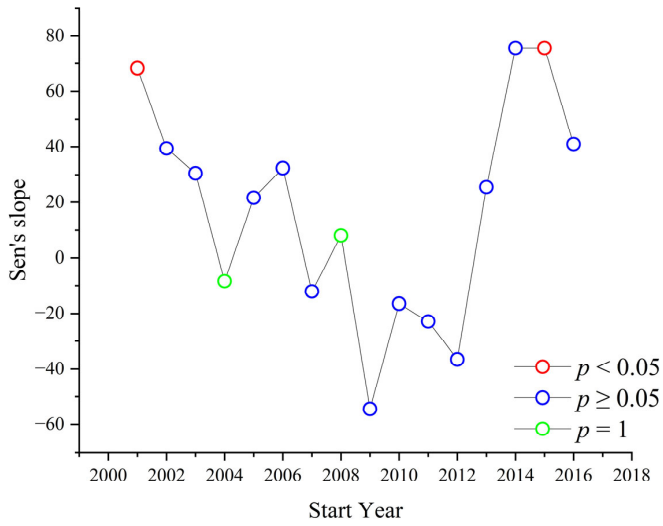


Figure 5. Sen's slope estimates from sliding window Mann–Kendall trend analysis of SOC stock (2001–2020).

Although some periods (such as 2002–2006, 2003–2007, and 2012–2016) had positive Sen's slope values, showing an upward tendency, the p was ≥ 0.05 for these windows, so the trend did not reach statistical significance and was more likely to reflect short-term fluctuations. In particular, in the windows 2004–2008 and 2008–2012, the $p = 1$, which further indicates that there was no detectable monotonic trend in SOC stock during these periods.

3.2.2. Spatial Variability Analysis

During 2001–2020, the mean SOC stock in the study area reached a maximum value of 1841.27 g C/m^2, with a multi-year average of 1683.98 g C/m^2 (Figure 6). At the regional scale, the mean total SOC stock amounted to 1.93 × 10^{14} g C/m^2, and the cumulative SOC stock over the 20-year period reached 3.85 × 10^{15} g C/m^2, indicating a sustained and substantial carbon sink capacity of the region in the long term.

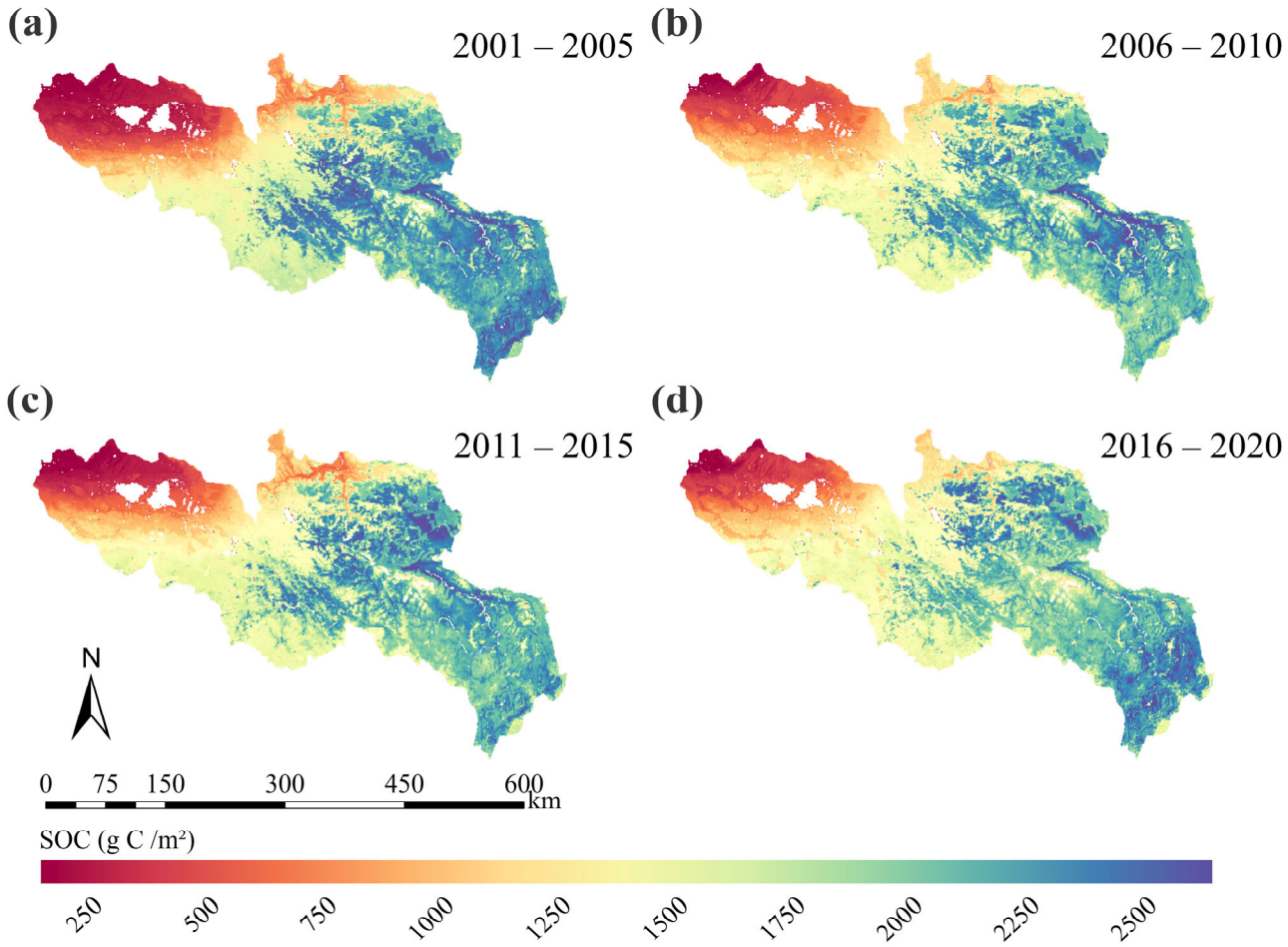


Figure 6. The SOC stock changes from 2001 to 2020. (**a**) Mean distribution of SOC stock (2001–2005); (**b**) mean distribution of SOC stock (2006–2010); (**c**) mean distribution of SOC stock (2011–2015); (**d**) mean distribution of SOC stock (2016–2020).

The analysis of SOC stock across different grassland types revealed pronounced spatial heterogeneity in both average levels and total accumulation (Table 3). Among all grassland types, the alpine meadow exhibited the highest total SOC stock, reaching 1.14 × 10^8 g C/m^2, which reflects the combined effect of its extensive spatial distribution of 82,870.3 km^2 and its relatively high mean SOC stock of 1566.3 g C/m^2. The cold temperate wet coniferous forest also demonstrated a notably high mean SOC stock, reaching 2025.9 g C/m^2, despite its smaller area, indicating its strong carbon storage capacity per unit land area. Meanwhile, ecosystems such as the cool temperate subhumid meadow

steppe and the cool temperate wet mixed forest, despite having relatively high mean SOC stock, had low total SOC stock due to their limited spatial extent, resulting in an overall small contribution to the regional SOC stock. Overall, the alpine meadow serves as the primary contributor to the regional SOC stock, whereas the cold temperate wet coniferous forest exhibits the highest mean SOC stock across all vegetation types.

Table 3. SOC stock of different grassland types.

Grassland Type	Grassland Area (km^2)	MIN		MAX		MEAN		STD		SUM	
		(g/kg)	(g C/m^2)	(g/kg)	(g C/m^2)	(g/kg)	(g C/m^2)	(g/kg)	(g C/m^2)	(g/kg × 10^3)	(g C/m^2 × 10^6)
Cool temperate subhumid meadow steppe	25.0	39.0	945.0	56.1	1147.5	41.6	1023.3	3.3	57.1	1.2	0.02
Cold temperate humid montane meadow	152.4	41.9	993.9	56.3	1387.7	48.3	1171.2	3.8	101.8	7.2	0.16
Cool temperate subhumid montane grassland	218.3	39.4	0.0	63.5	1568.8	45.8	1096.3	4.1	152.3	10.2	0.21
Alpine meadow	82,870.3	23.1	0.0	103.2	2456.2	68.3	1566.3	21.3	465.2	5760.5	114.15
Cold temperate wet coniferous forest	29,678.5	42.9	0.0	103.7	2498.1	87.6	2025.9	12.5	290.0	2634.4	52.88
Cool temperate wet mixed coniferous and broad-leaved forest	4.6	54.4	1211.7	56.7	1341.0	55.6	1300.0	0.9	51.8	0.2	0.01

In this study, we examined the trends in SOC stock across different grassland types in the source region of the Yellow River and quantified the proportion of significant changes for each type during 2001–2020 (Figure 7). The results are as follows.

The maximum interannual variations in SOC stock for the cool temperate subhumid meadow steppe, cold temperate humid montane meadow, and cool temperate subhumid montane grassland were 692.18, 866.99, and 711.52 g C/m^2, respectively, with corresponding SOC stock ranges of 949.70, 1095.73, and 1000.08 g C/m^2. These three grassland types exhibited relatively consistent interannual fluctuation patterns with comparable intensities, among which the cold temperate humid montane meadow showed the greatest variability.

The cool temperate wet mixed coniferous and broad-leaved forest exhibited a maximum interannual variation of 978.40 g C/m^2 and a range of 1068.86 g C/m^2. Although its fluctuation magnitude was comparable to that of the three grassland types, SOC stock in this type remained relatively stable over multiple consecutive years, overall exhibiting a variation trend distinct from other grassland types.

In contrast, the alpine meadow showed a smaller range and maximum interannual variation of 393.51 g C/m^2 and 220.45 g C/m^2, respectively, while the corresponding values for the cold temperate wet coniferous forest were 256.48 g C/m^2 and 235.12 g C/m^2. These two grassland types showed markedly lower variability in SOC stock and overall greater stability.

At the regional scale, interannual variations in SOC stock were significantly and positively correlated with annual precipitation ($r = 0.63$, $p = 0.0026$), but significantly and negatively correlated with annual maximum air temperature ($r = -0.46$, $p = 0.0432$). Years with higher precipitation (e.g., 2005 and 2009) generally corresponded to higher SOC stock levels, whereas years characterized by reduced precipitation or elevated maximum temperature (e.g., 2006 and 2013) were associated with relatively lower SOC stock. These temporal patterns indicate that interannual climate variability plays an important role in regulating SOC stock dynamics in the study area.

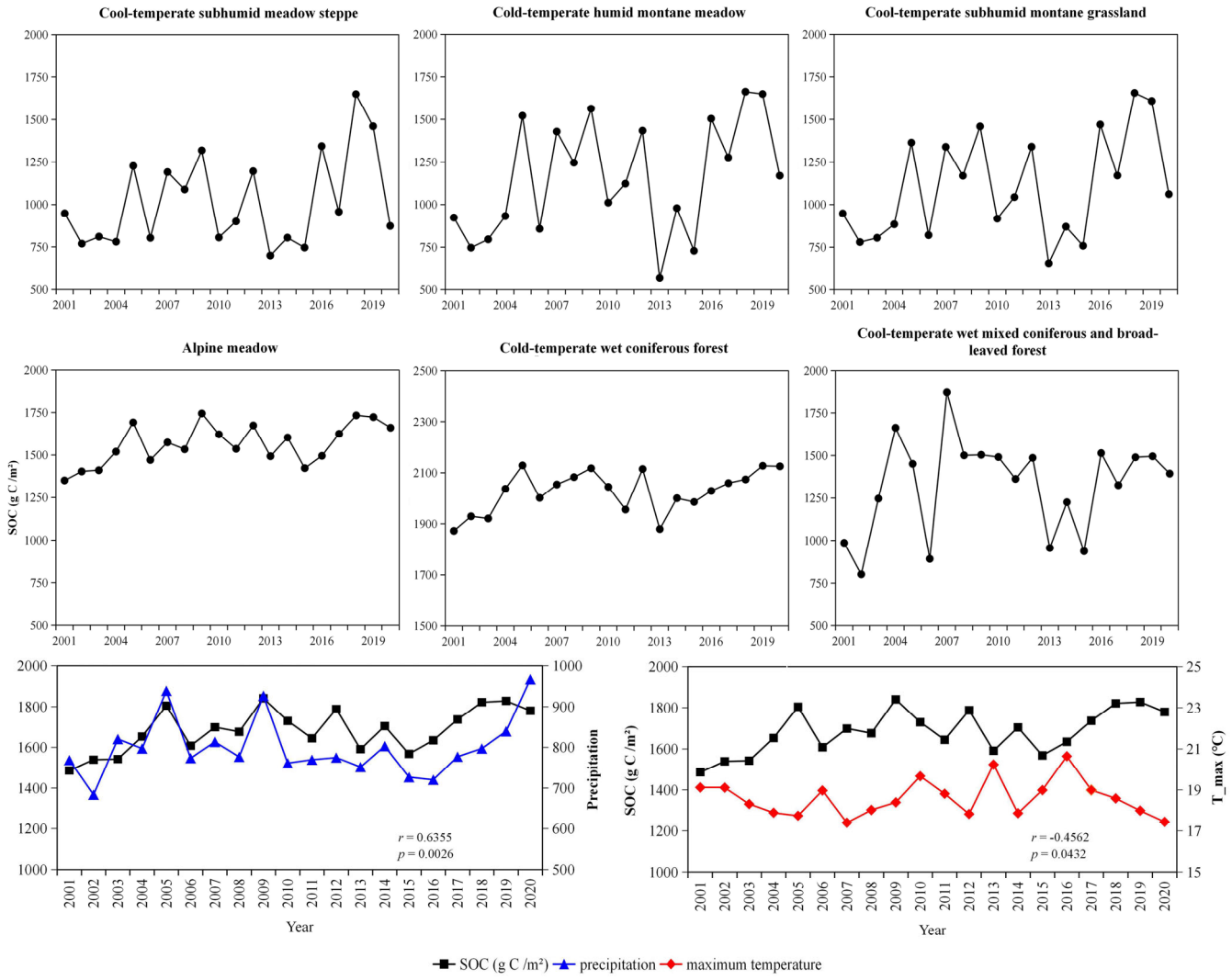


Figure 7. SOC stock trends of different grassland types.

The magnitude of significant changes in SOC stock varied markedly among different grassland types; however, all major types exhibited an overall increasing trend, indicating a strong carbon sink function in the study area (Table 4). Cold temperate humid montane meadow and cool temperate subhumid montane grassland showed the highest rates of carbon accumulation, with mean Sen's slopes reaching 24.00 g C/m^2/yr and 17.94 g C/m^2/yr, respectively. Although the mean SOC stock of these two grassland types was relatively low (approximately 1100 g C/m^2), they are currently in a phase of rapid carbon accumulation. Alpine meadow was the most widely distributed grassland type in the study area, covering more than 8×10^4 km^2. Approximately 24.7% of this area exhibited a statistically significant increase in SOC stock. Alpine meadow showed a moderate accumulation rate, with a mean Sen's slope of 9.76 g C/m^2/yr, and maintained a relatively high background SOC stock (approximately 1560 g C/m^2), thereby playing a dominant role in the regional carbon balance.

Table 4. Significant changes in soil organic carbon stock across different grassland types.

Grassland Type	Increasing Significant Ratio	Decreasing Significant Ratio	Mean Slope
Cool temperate subhumid meadow steppe	0.000	0.000	9.909
Cold temperate humid montane meadow	0.089	0.000	23.998
Cool temperate subhumid montane grassland	0.048	0.000	17.942
Alpine meadow	0.247	0.026	9.761
Cold temperate wet coniferous forest	0.119	0.006	5.585
Cool temperate wet mixed coniferous and broad-leaved forest	0.000	0.000	7.938

In contrast, cold temperate wet coniferous forest exhibited a comparatively slower increase in SOC stock, characterized by a mean Sen's slope of 5.59 g C/m^2/yr, but had the highest average SOC stock (approximately 2026 g C/m^2), indicating that this grassland type is more focused on long-term and stable carbon storage. Due to their limited spatial extent, results for cool temperate subhumid meadow steppe and cool temperate wet mixed coniferous and broad-leaved forest were used for descriptive purposes only.

3.3. Driving Mechanisms

At the regional scale, the factor detector revealed that the spatial variation of SOC stock was primarily driven by meteorological factors (Figure 8). Annual precipitation (AP) showed the strongest explanatory power $q = 0.775$, followed by latitude (Lat; q = 0.368) and accumulated temperature (AT; $q = 0.324$). Topographic slope exhibited a moderate effect ($q = 0.156$), whereas the remote sensing indices b7-W ($q = 0.110$) and B-W ($q = 0.029$), as well as soil pH ($q = 0.050$), contributed relatively little when considered individually. All factors passed the significance test ($p < 0.001$), although their explanatory powers differed markedly.

The interaction detector further demonstrated that the combined effects of paired factors generally enhanced the explanatory power for SOC spatial variation compared with single factors (Figure 8b, lower-right triangular matrix). According to the Geodetector criteria, interactions were classified as bilaterally enhanced when the interaction q value exceeded the maximum of the two individual q values but remained lower than their sum and as nonlinearly enhanced when the interaction q value exceeded the sum of the individual effects. Strong bilateral enhancement was observed for interactions involving AP, such as AP ∩ AT ($q = 0.826$), AP ∩ Lat ($q = 0.803$), and AP ∩ slope ($q = 0.786$). Meanwhile, nonlinear enhancement frequently occurred when factors with relatively low explanatory power interacted with stronger drivers, as exemplified by b7-W ∩ AT ($q = 0.453$), AT ∩ slope ($q = 0.526$), and AP ∩ pH ($q = 0.831$). The ecological detector results are presented in the upper-left triangular matrix of Figure 8b, where Y indicates that the difference in explanatory power between paired factors passes the significance test.

Risk detector analysis showed significant differences in SOC stock across factor-different strata of each factor. SOC stock increased markedly with AP, rising from approximately 730 g C/m^2 in low-precipitation areas (261–354 mm) to over 2060 g C/m^2 in high-precipitation areas (>846 mm). AT exhibited a nonlinear pattern, with lower SOC stock at intermediate temperature ranges and higher values at both low and high accumulated temperature levels. SOC stock peaked at mid-latitudes (32.3–32.7°) and declined toward

higher latitudes. Topographic slope showed an increasing trend up to moderate slopes (17.6–20.4°), after which SOC stock slightly decreased.

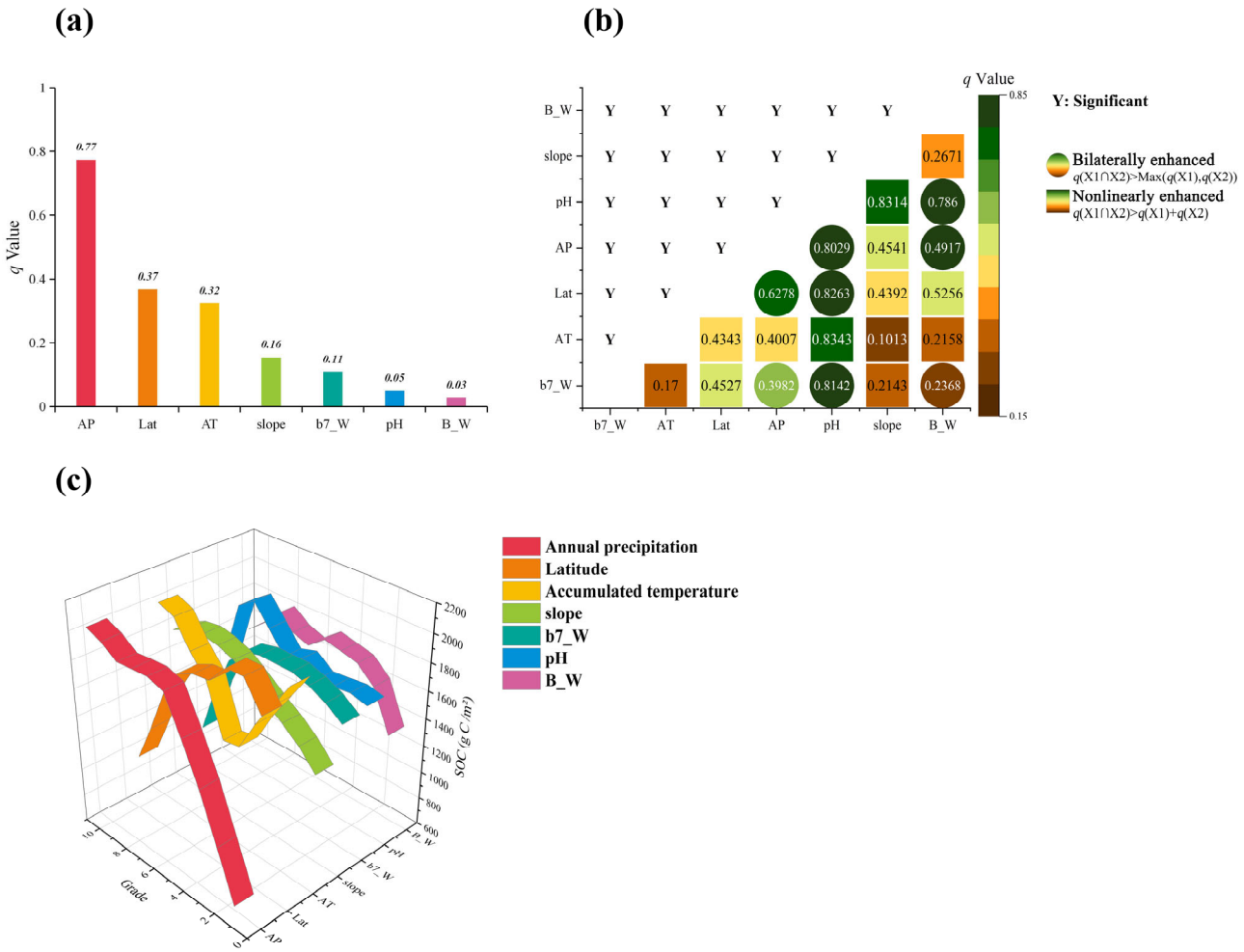


Figure 8. Geographical detector analysis. (**a**) Factor detector; (**b**) interaction detector and ecological detector; (**c**) risk detector.

By comparison, soil pH and remote sensing indices showed relatively weaker effects on SOC stock, with smaller differences across strata. SOC stock increased with slope from very gentle slopes (1.92–6.54°, 1325.37 g C/m^2) to moderate slopes (17.60–20.40°, 1880.98 g C/m^2), followed by a slight decline at steeper slopes (1806.19 g C/m^2), indicating a limited and non-monotonic topographic influence. SOC stock showed moderate variation across soil pH strata, increasing toward intermediate pH levels and reaching a maximum of 1955.85 g C/m^2 at pH 6.40–6.57, followed by a marked decline at higher pH ranges, without a clear or consistent gradient. Remote sensing indices exhibited a similar "high in the middle and low at the extremes" pattern: SOC stock associated with b7-W peaked at intermediate values (1759.91 g C/m^2) and declined sharply toward higher ranges (973.25 g C/m^2), while SOC stock related to B-W reached its maximum (1787.09 g C/m^2) at mid-range values and decreased at both ends (1568.00 g C/m^2). Overall, these factors showed weaker and less stable stratified responses compared with climatic drivers.

3.4. Carbon Sequestration Value

In this study, the carbon sequestration value was estimated from the perspective of opportunity cost, representing the social loss avoided by preventing the emission of one ton of carbon into the atmosphere [101–103]. Following the guidelines of the National

Development and Reform Commission of China, the carbon price was set at 10 USD per ton of carbon.

Under this carbon price, the cumulative SOC stock carbon sequestration value in the study area from 2001 to 2020 was approximately 3.80×10^{10} USD, indicating substantial ecological and economic benefits. On a per area basis, the cumulative value was about 3,367.96 USD/ha, with an average annual value of 168.40 USD/ha/yr. These results suggest that grassland carbon sequestration contributes significantly to regional carbon cycling in terms of total stock, while also providing considerable economic returns per unit area.

The economic value of SOC stock varied significantly among different grassland types (Table 5). The alpine meadow had the largest total carbon value (129.80×10^7 USD), with high cumulative and annual per area values of 3,132.52 USD/ha and 156.63 USD/ha/yr, respectively, reflecting its dominant role in the regional carbon pool. The cold temperate wet coniferous forest showed the highest per area value, with cumulative and annual values of 4,051.88 USD/ha and 202.59 USD/ha/yr, respectively, despite a lower total value (60.13×10^7 USD). The cool temperate wet mixed coniferous and broad-leaved forest, although having the smallest total value (0.006×10^7 USD), maintained relatively high per area values (2600.07 USD/ha cumulative; 130.00 USD/ha/yr annual), indicating substantial economic efficiency within its limited area. In contrast, the cool temperate subhumid meadow steppe contributed the least to the regional carbon pool, with the lowest total (0.026×10^7 USD) and per area values (2046.60 USD/ha cumulative; 102.33 USD/ha/yr annual). The cold temperate humid montane meadow and cool temperate subhumid montane grassland occupied intermediate levels, with total values of 0.178×10^7 USD and 0.239×10^7 USD and cumulative per area values of 2,342.47 USD/ha and 2,192.68 USD/ha, providing moderate support to the regional carbon stock.

Table 5. Economic value of SOC stock across different grassland types.

Grassland Type	Total Carbon Value (USD $\times 10^7$ tC)	Cumulative Per Area Value (USD/ha)	Average Annual Per Area Value (USD/ha/yr)
Cool temperate subhumid meadow steppe	0.026	2046.60	102.33
Cold temperate humid montane meadow	0.178	2342.47	117.12
Cool temperate subhumid montane grassland	0.239	2192.68	109.63
Alpine meadow	129.796	3132.52	156.63
Cold temperate wet coniferous forest	60.127	4051.88	202.59
Cool temperate wet mixed coniferous and broad-leaved forest	0.006	2600.07	130.00

Note: Economic values were calculated based on SOC stock (g C/m^2) using a carbon price of 10 USD/t C.

In summary, the economic value of SOC stock varied markedly among grassland types. The alpine meadow dominated the total carbon value due to its large stock, serving as the primary component of the regional carbon pool. The cold temperate wet coniferous forest exhibited a clear advantage in per area value. Although the cool temperate wet mixed coniferous and broad-leaved forest had a limited total value, its per area value was relatively high, indicating substantial economic efficiency within its restricted distribution.

In contrast, the cool temperate subhumid meadow steppe contributed minimally to the regional carbon pool.

4. Discussion

4.1. Model Performance and Comparison

This study compared the performance of multiple modeling approaches and variable sets in estimating SOC stock. Model performance varied across methods. In PLS, the SR variable set yielded the best results (R^2 = 0.50, RMSE = 38.329). RF performed best with LASSO (R^2 = 0.45, RMSE = 39.964), while SVM achieved its highest accuracy with LASSO (R^2 = 0.53, RMSE = 36.190). LGBM showed the highest overall accuracy, particularly with SR (R^2 = 0.51, RMSE = 36.863). Across the same variable set, LGBM and SVM generally outperformed RF and PLS, highlighting their ability to capture complex relationships between SOC and multiple environmental factors. Variable selection also substantially influenced performance: SR and LASSO sets improved prediction accuracy and stability compared with RR and CS sets.

LGBM demonstrated the greatest stability across variable sets, with R^2 around 0.50 ($\pm$0.02) and RMSE between 36.863 and 39.026, whereas PLS (R^2: 0.08–0.50), RF (R^2: 0.40–0.45), and SVM (R^2: 0.43–0.53) fluctuated more. This indicates LGBM's robust generalization in complex multi-factor systems [104–107].

The LASSO variable set generally outperformed others, highlighting the importance of eliminating redundant features and emphasizing key drivers, consistent with prior studies [108–110]. Its advantage is pronounced in alpine grasslands with strong climate gradients, complex topography, and high soil heterogeneity [111,112].

Among all combinations, SVM with LASSO achieved the highest accuracy and lowest error, reflecting SVM's capability to capture complex interactions and LASSO's effective feature selection. This synergy enhances both predictive performance and model interpretability, reliably representing SOC spatial distribution.

Overall, machine learning results reveal that high-altitude SOC spatial patterns are jointly influenced by temperature, precipitation, slope, and soil properties [113,114]. Differences among models underscore the significance of factor interactions and demonstrate that variable-selection-based modeling better captures SOC formation mechanisms and spatial heterogeneity. LGBM, meanwhile, maintained robustness across variable sets, showing strong transferability. Integrating machine learning with careful variable selection thus improves SOC estimation accuracy and interpretability, offering a practical approach for understanding environmental drivers of carbon stocks in alpine grasslands [115,116].

4.2. Spatiotemporal Distribution Characteristics

From 2001 to 2020, SOC stock in the study area exhibited a significant increasing trend (τ = 0.389, p = 0.018), with an average annual rise of approximately 11.69 g C/m^2, indicating an overall enhancement of regional carbon sequestration. This finding aligns with previous studies on long-term SOC accumulation in the Qinghai–Tibet Plateau and alpine grasslands [117,118]. The observed trend may be attributed to increased vegetation productivity under warming conditions [119], as well as ecological restoration measures such as grazing exclusion and grassland rehabilitation [120–122]. Annual SOC stock values fluctuated between 1486.11 and 1841.27 g C/m^2, with relatively stable interquartile ranges, indicating consistent spatial distribution patterns despite inter-annual variability.

Sliding window analysis revealed phased changes in SOC. Significant increases occurred during 2001–2005 and 2015–2019, whereas other periods were more likely to reflect short-term fluctuations rather than persistent trends. These results are consistent with the relationships between SOC stock and total precipitation as well as maximum temperature

across the study region. During the periods of 2001–2005 and 2015–2019, SOC stock showed a sustained increase with increasing precipitation and decreasing maximum temperature, whereas in other periods, it exhibited more fluctuating variations. This pattern reflects the influence of meteorological factors, particularly precipitation and temperature. In addition, SOC growth may also be associated with policy interventions, including grazing bans and improvements in grassland management practices [123–127].

SOC varied among grassland types. Alpine meadow showed the highest proportion of significant increase (24.7%), suggesting strong potential for carbon accumulation. In contrast, cool temperate subhumid meadow steppe and cool temperate wet mixed coniferous and broad-leaved forest exhibited little change, maintaining relative stability. These differences likely reflect variations in vegetation composition, soil texture, and hydrothermal conditions among grassland types [128].

Overall, SOC in the Yellow River Source Area increased significantly from 2001 to 2020, exhibiting phased, spatially heterogeneous, and clustered changes. Climate variability, grassland type differences, and human activities are key drivers of these spatiotemporal patterns.

4.3. Driving Mechanisms Analysis

Through correlation and regression analyses, seven core factors with significant influence on SOC stock were identified: climatic factors (AT, AP), topographic factors (Lat, Slope), soil property (pH), and remote sensing indices (b7-W, B-W). These factors were consistently selected across three regression methods, indicating robust influence on SOC and aligning with previously reported key drivers in alpine grasslands [129].

Among these factors, annual precipitation was the most influential. Both correlation and regression analyses showed a significant positive relationship between annual precipitation and SOC. Factor detector analysis confirmed its dominant explanatory power (q = 0.775). When interacting with other major drivers, such as accumulated temperature or latitude, the q values often exceeded 0.8, indicating pronounced bilateral or nonlinear enhancement effects. Although increased soil moisture and rising temperature are generally considered to stimulate microbial activity and accelerate organic matter decomposition, potentially leading to SOC losses [119,130]. Studies on the Qinghai–Tibet Plateau show that, at shorter temporal scales, low to moderate frequencies of extreme precipitation may enhance SOC decomposition, whereas higher precipitation frequencies or persistently moist conditions suppress decomposition and favor the accumulation of particulate or total SOC [55,130]. At broader temporal and spatial scales, SOC content is positively correlated with soil moisture and above- and belowground biomass but negatively correlated with soil temperature [131], consistent with the relationships observed in this study, suggesting that wetter conditions enhance plant carbon inputs while constraining decomposition. It should also be noted that complex climatic dynamics and rugged topography in the study region amplify surface runoff and soil erosion during intense rainfall events, and increasing precipitation extremes may offset potential SOC gains, indicating that interactions between extreme precipitation and topography constitute an important source of environmental vulnerability [132,133].

Accumulated temperature had moderate explanatory power. Its effect was limited in single-factor analyses but exhibited enhancement when interacting with other factors [15]. This interaction is driven by the fact that, in alpine regions, temperature regulates soil freeze–thaw processes and active layer thickness [15,134], thereby influencing soil moisture availability and microbial activity [135]. Given these tightly intertwined physical and biological processes, the effects of these drivers are likely to be underestimated if assessed solely from a single-factor perspective.

Latitude ranked second in explanatory power. Contrary to the typical latitudinal climate gradient effect, where decreasing temperature and increasing moisture with latitude promote SOC accumulation [136,137], in the study area, SOC decreased with latitude. This pattern reflects the combined influence of vegetation coverage, soil properties, permafrost degradation, and altitude [138], corroborating previous findings on regional SOC distribution [15].

Slope exhibited limited explanatory power in single-variable correlation ($r = -0.04$, $p = 0.33$) but was retained in stepwise, ridge, and LASSO regressions, with factor detector $q = 0.156$. Risk detector results indicated higher SOC on gentle-to-moderate slopes and lower SOC on very flat areas, likely reflecting indirect effects of slope on water convergence, erosion, and vegetation distribution. Prior studies suggest slope mainly modulates SOC indirectly rather than acting as a direct control factor [139,140], supporting its limited yet reasonable explanatory power.

Soil pH had weak explanatory power across methods. Risk detector analysis showed minimal stratified effect [141]. Significant impacts are generally observed only under extreme acidic or alkaline conditions [142,143]. Given the study area's generally non-extreme pH range, the limited effect on SOC aligns with expectations.

Remote sensing indices (b7-W, B-W) also showed low explanatory power. The risk detector revealed a hump-shaped relationship, with SOC peaking at moderate vegetation coverage. This pattern likely arises because low coverage limits organic input, while very high coverage increases decomposition and nutrient cycling pressure, reducing SOC accumulation [144–146]. Similar "intermediate–optimum" patterns have been observed in remote sensing-based grassland carbon studies [147].

Overall, combining variable selection and factor detector analyses indicates that SOC spatial variability in the Yellow River Source Area is primarily driven by climatic factors, with annual precipitation exerting the strongest influence, followed by accumulated temperature and latitude. Slope plays a limited but robust role through interactions with climatic factors. Soil pH and remote sensing bands exhibit the weakest explanatory power, contributing only minor regulatory effects. Notably, multi-factor interactions significantly enhance explanatory power, particularly the coupled effects of hydrothermal conditions, highlighting the complex mechanisms underlying SOC distribution. These findings advance understanding of SOC dynamics in alpine grasslands and provide a scientific basis for predicting SOC responses under climate change and for regional grassland carbon management.

4.4. Policy Implications: Carbon Sequestration Value

This study further demonstrates that differences in carbon stock and economic value among grassland types are reflected not only in total quantity but also in quality and efficiency, underscoring the critical role of alpine grasslands in China's national "dual carbon" strategy. These findings have important implications for regional carbon management and ecological compensation policies.

From a land use and management perspective, the Yellow River Source Area on the Qinghai–Tibet Plateau is dominated by extensive grazing and small-scale subsistence agriculture [148,149]. Livestock production mainly relies on indigenous species such as yaks and Tibetan sheep [150], with grazing practices mainly characterized by grazing bans, seasonal rest grazing, and fenced, parcel-based rotational grazing [151,152]. Crop cultivation mainly includes barley and oats and relies on traditional cultivation practices [153]. These land use patterns, together with the cumulative grazing pressure in some areas, tend to induce grassland degradation, soil disturbance, and erosion, thereby constraining the accumulation and stability of soil organic carbon [154]. In this context, the regional carbon sequestration functions are maintained and restored through a comprehensive manage-

ment system comprising several major initiatives, such as the Sanjiangyuan Ecological Protection Project (https://www.ndrc.gov.cn/, accessed on 16 December 2025), the Grazing Ban Project (http://www.moa.gov.cn/, accessed on 16 December 2025), and the Grassland Ecological Reward Policy (https://www.ndrc.gov.cn/, accessed on 16 December 2025), among others. This synergy between community-based management and conservation-oriented policy interventions—encompassing livestock reduction, ecological compensation, and habitat restoration—is essential for sustaining the regional carbon pool.

Alpine meadows, owing to their extensive distribution [155], rank highest in total stock and overall value, highlighting their dominant role in regional carbon stock and carbon-related economic benefits [156,157]. Policy should prioritize the protection of their ecological integrity, maintaining carbon sequestration functions through measures such as degraded grassland restoration and grazing restriction, and integrating them into regional carbon accounting frameworks.

In contrast, cold temperate wet coniferous forests, though limited in area, exhibit the highest average carbon density and per area value, reflecting a clear "quality advantage" and significant potential for carbon sequestration and economic development. These differentiated characteristics are critical for regional carbon stocks and carbon market valuation [158,159]. Policy instruments such as grassland carbon credits or ecological compensation funds [160–162] could incentivize local governments and herders to conserve high-carbon-density grasslands, thereby increasing the economic attractiveness of carbon management.

Overall, these results reveal the differentiated ecological and carbon stock functions of grasslands and provide scientific guidance for grassland resource management and carbon trading policy. In practice, management strategies should balance the contribution of large-area grasslands with the high per area efficiency of specific types to optimize regional carbon sequestration. In addition, greater emphasis should be placed on policy mechanisms that contribute to the protection of ecologically sensitive and significant areas, such as the Yellow River Source Area [163]. Payments for environmental and ecosystem services (PES) can promote sustainable land use practices by incorporating the ecological benefits of soil carbon sequestration, grassland conservation, and hydrological regulation into economic incentive schemes [164,165]. Furthermore, under a One Health framework, environmental integrity, human livelihoods, and animal health should be jointly considered [166], and conservation-oriented, integrated governance measures should be adopted to enhance socio-ecological system resilience and ensure the long-term stability of the Yellow River Source Area under increasing pressures from climate change and human activities [167].

4.5. Future Perspectives

Future assessments of SOC stock dynamics in alpine grassland ecosystems will benefit from continued methodological advances and data integration. Incorporating higher-spatial-resolution satellite imagery (e.g., Sentinel-2 at 10 m or finer resolution) together with more intensive and standardized field sampling will improve the representation of fine-scale spatial heterogeneity. In addition, integrated frameworks that combine multi-source remote sensing, deep learning-based spatial interpolation, and frequent in situ monitoring offer strong potential to refine site-level estimates and further enhance the accuracy of carbon sequestration modeling across complex highland regions such as the Yellow River Source Area.

5. Conclusions

This study compared the performance of different modeling approaches for estimating SOC stocks, revealing that machine learning models generally outperform traditional regression models. Among them, the SVM model combined with the LASSO-selected variable set achieved the best performance on the test dataset (R^2 = 0.53, RMSE = 36.190), demonstrating that rational variable selection coupled with advanced algorithms can effectively enhance the spatial prediction of SOC.

In terms of spatiotemporal patterns, SOC showed a significant increasing trend from 2001 to 2020 (approximately 11.69 g C/m^2 per year), accompanied by stage-wise fluctuations and pronounced spatial clustering, with notable differences among grassland types.

Driver analysis further identified the core factors controlling SOC spatial heterogeneity. Annual precipitation exhibited the strongest explanatory power, followed by latitude and temperature, while multi-factor interactions significantly amplified SOC spatial predictability, highlighting the dominant role of hydrothermal conditions and climate–topography coupling in the carbon cycle of alpine grasslands. In contrast, soil and remote sensing variables contributed minimally, mainly influencing SOC at local scales. Overall, SOC spatial patterns emerge from the combined and interdependent effects of multiple environmental drivers rather than any single controlling factor.

Regarding the carbon sink value, alpine meadow grasslands contributed the highest total stock, whereas cold temperate wet coniferous forest grasslands exhibited higher per unit area value, reflecting distinct quantity–quality characteristics.

Overall, this study not only validates the effectiveness of modeling and variable selection in SOC estimation but also advances understanding of the driving mechanisms of SOC in the Yellow River source region's alpine grasslands, providing a scientific basis for future grassland carbon management, carbon market allocation, and climate change mitigation strategies.

Author Contributions: Conceptualization, Z.Z. and J.S.; methodology, Z.Z. and H.L.; software, Z.Z., J.S. and H.M.; validation, Z.Z. and J.S.; formal analysis, Z.Z. and J.S.; investigation, Z.Z., J.S. and H.M.; resources, H.L.; data curation, Z.Z. and H.M.; writing—original draft preparation, Z.Z.; writing—review and editing, Z.Z., J.S. and X.W.; visualization, Z.Z. and X.W.; supervision, H.L.; project administration, H.L.; funding acquisition, H.L. All authors have read and agreed to the published version of the manuscript.

Funding: This research was funded by the National Natural Science Foundation of China (31772666).

Data Availability Statement: All data used in this study are included in the article.

Acknowledgments: The authors express their gratitude to the editor and the anonymous reviewers for their insightful comments and constructive feedback, which significantly enhanced the quality of this paper.

Conflicts of Interest: The authors declare no conflicts of interest.

Appendix A. Calculation Methods, Data Sources, and Correlation Analysis for SOC and Environmental Variables

Table A1. Calculation Methods of Relevant Indices.

Remote Sensing Indicators	Variable Interpretation	Calculation Method	Reference
BI	Brightness Index	$\sqrt{Red^2 + NIR^2}$	[168]
CI	Coloration Index	$\frac{Red-Green}{Red+Green}$	[168]

Table A1. *Cont.*

Remote Sensing Indicators	Variable Interpretation	Calculation Method	Reference
DVI	Difference Vegetation Index	$NIR - Red$	[169]
EVI	Enhanced Vegetation Index	$\frac{2.5\,(NIR-Red)}{1+NIR+6Red-7.5Blue}$	[170]
TVI	Transformed Vegetation Index	$(NDVI + 0.5)^{0.5}$	[171]
MSAVI	Modified Soil-Adjusted Vegetation Index	$\frac{2NIR+1-\sqrt{(2NIR+1)^2-8(NIR-Red)}}{2}$	[172]
NDVI	Normalized Difference Vegetation Index	$\frac{NIR-Red}{NIR+Red}$	[171]
RVI	Ratio Vegetation Index	$\frac{NIR}{Red}$	[173]
NDSI	Normalized Difference Soil Index	$\frac{SWIR-Green}{SWIR+Green}$	[174]
NDWI	Normalized Difference Water Index	$\frac{Green-NIR}{Green+NIR}$	[175]
NDVGI	Normalized Difference Vegetation Green Index	$\frac{NIR-Green}{NIR+Green}$	[176]
OSAVI	Optimized Soil-Adjusted Vegetation Index	$\frac{NIR-Red}{NIR+Red+0.16}$	[177]
SCI	Soil Color Index	$3NIR + Red - Green - 3Blue$	[178]
SAVI	Soil-Adjusted Vegetation Index	$\frac{NIR-Red}{(NIR+Red+L)}(1+L)$	[179]
SATVI	Soil-Adjusted Total Vegetation Index	$\frac{SWIR_1+Red}{(SWIR_1+Red+L)}(1+L) - \frac{SWIR_2}{2}$	[180]
A		$\frac{b_5}{b_7}$	[181]
B		$\frac{b_5-b_7}{b_5+b_7}$	[181]
C		$\frac{b_7}{b_5}$	[181]
D		$\frac{b_7}{b_2}$	[182]
E		$b_2 - b_7$	[181]

Note: NIR, Red, Blue, and Green represent the near-infrared, red, blue, and green bands, respectively. In the SAVI and SATVI formulas, $L = 0.5$. In the SATVI formula, $SWIR_1$ corresponds to the short-wave infrared band (Band 6 in MODIS products), and $SWIR_2$ corresponds to the short-wave infrared band 2 (Band 7 in MODIS products). In addition, b_2, b_5, and b_7 correspond to Bands 2, 5, and 7 in the MOD09A1 products, respectively.

Table A2. Environmental Variable Data Sources.

	Variable	Unit	Resolution	Data Sources	Annotation
SOC	Soil organic carbon	g/kg		Measured	
Topographic Factors	Longitude (Lon)		–	GPS	Real-time sampling by GPS devices
	Latitude (Lat)		–	GPS	Real-time sampling by GPS devices
	Altitude (Alt)	m	1 km	SRTM 90m DEM Digital Elevation Database (https://srtm.csi.cgiar.org/, accessed on 20 December 2025)	
	Aspect (Asp)	°	1 km	Calculate from DEM using ArcGIS Pro	
	Slope	°	1 km		

Table A2. *Cont.*

	Variable	Unit	Resolution	Data Sources	Annotation
Climatic Factors	Accumulated temperature (AT)	°C	1 km	Daily data set of surface climate data in China (https://data.cma.cn/, accessed on 20 December 2025)	≥0 °C
	Annual mean temperature (AMT)	°C	1 km		
	Annual precipitation (AP)	mm	1 km		
	LsTD–S	°C	1 km	MOD11A2	Daytime ground temperature in summer
	LsTD-W	°C	1 km		Daytime ground temperature in winter
	LsTN-S	°C	1 km		Ground temperature at night in summer
	LsTN-W	°C	1 km		Ground temperature at night in winter
Soil Physicochemical Properties	Clay1	%	1 km	Big Data Center of Sciences in Cold and Arid Regions (http://bdc.casnw.net/yyzc/sj/, accessed on 20 December 2025) soil characteristic data set	(0–30 cm) Clay content
	Clay2	%	1 km		(30–100 cm) Clay content
	Sand1	%	1 km		(0–30 cm) Sand content
	Sand2	%	1 km		(30–100 cm) Clay content
	sand1/clay1	%	1 km		(0–30 cm) Soil sand–clay ratio
	snad2/clay2	%	1 km		(30–100 cm) Soil sand–clay ratio
	pH		250 m	SoilGrids250m 2.0 (https://soilgrids.org/, accessed on 20 December 2025)	Soil pH value
	BD	(kg/m^3)	250 m		Bulk density
Vegetation Factors	NPP	KgC/m^2	1 km	MOD17A3HGF	Annual net primary productivity
	EVI		250 m	MOD13Q1 band calculated	Enhanced vegetation index in summer and winter
	NDVI		250 m		Normalized vegetation index in summer and winter
	TVI		250 m		Conversion vegetation index in summer and winter
	BI		1 km		Brightness index in summer and winter
	DVI		1 km		Differential vegetation index in summer and winter
	MSAVI		1 km		Improved soil-adjusted vegetation index in summer and winter
	NDSI		1 km		Normalized difference soil index in summer and winter
	NDWI		1 km		Normalized differential water index in summer and winter
	NDVGI		1 km		Normalized difference vegetation greenness index in summer and winter

Table A2. *Cont.*

	Variable	Unit	Resolution	Data Sources	Annotation
Vegetation Factors	OSAVI		1 km	MOD13Q1 band calculated	Optimal soil-adjusted vegetation index in summer and winter
	RVI		1 km		Ratio of the vegetation coefficient in summer and winter
	SATVI		1 km		Soil-adjusted total vegetation index in summer and winter
	SAVI		1 km		Soil-adjusted vegetation index in summer and winter
	SCI		1 km		Soil color index in summer and winter
Remote Sensing Indices	A		500 m	MOD09A1 dataset	Band in summer and winter
	B		500 m		
	C		500 m		
	D		500 m		
	E		500 m		
	b1		500 m		
	b2		500 m		
	b3		500 m		
	b4		500 m		
	b5		500 m		
	b6		500 m		
	b7		500 m		
	Far		1 km	MOD15A2 dataset	Photosynthetic effective radiation in summer and winter
	Lai		1 km		Leaf area index in summer and winter
	BLUE		250 m	MOD13Q1 dataset	Blue band reflectance in winter
	MIR		250 m		Mid-infrared reflectance in winter
	NIR		250 m		Near-infrared reflectance in winter
	RED		250 m		Red band reflectance in winter

Table A3. Pearson's Correlation Analysis between SOC and topographic, climatic, and soil physico-chemical factors.

	Variable	Correlation Coefficient	*p* Value		Variable	Correlation Coefficient	*p* Value
Topographic Factors	Lon	0.231 **	0.00	Soil Physico-chemical Properties	clay1	0.126 **	0.00
	Lat	−0.357 **	0.00		clay2	0.177 **	0.00
	Alt	−0.03	0.52		sand1	−0.03	0.54
	Asp	−0.04	0.36		sand2	−0.03	0.41
	Slope	−0.04	0.33		sand1/clay1	0.04	0.38
Climatic Factors	AT	−0.294 **	0.00		sand2/clay2	0.06	0.11
	AMT	−0.126 **	0.00		pH	−0.244 **	0.00
	AP	0.222 **	0.00		BL	0.02	0.66
	LsTD-S	−0.110 **	0.01				
	LsTD-W	−0.105 **	0.01				
	LsTN-S	−0.02	0.64				
	LsTN-W	−0.271 **	0.00				

Note: The suffix -S denotes summer indicators, and -W denotes winter indicators. ** $p \leq 0.01$.

Table A4. Pearson's Correlation Analysis between SOC and vegetation factors.

Variable	Correlation Coefficient	*p* Value	Variable	Correlation Coefficient	*p* Value
NPP	0.094 *	0.02	NDWI-S	0.084 *	0.04
EVI-S	0.108 **	0.01	NDWI-W	−0.279 **	0.00
EVI-W	0.05	0.23	NDVGI-S	0.134 **	0.00
NDVI-S	0.129 **	0.00	NDVGI-W	0.189 **	0.00
NDVI-W	0.173 **	0.00	OSAVI-S	0.135 **	0.00
TVI-S	0.129 **	0.00	OSAVI-W	0.145 **	0.00
TVI-W	0.167 **	0.00	RVI-S	−0.088 *	0.03
BI-S	0.150 **	0.00	RVI-W	−0.182 **	0.00
BI-W	−0.278 **	0.00	SATVI-S	0.081 *	0.04
DVI-S	0.111 **	0.01	SATVI-W	−0.279 **	0.00
DVI–W	0.06	0.13	SAVI-S	0.129 **	0.00
MSAVI-S	0.128 **	0.00	SAVI–W	0.113 **	0.01
MSAVI–W	0.100 **	0.01	SCI-S	0.079 *	0.05
NDSI-S	−0.06	0.15	SCI–W	−0.184 **	0.00
NDSI–W	0.086 *	0.03			

Note: * $p \leq 0.05$; ** $p \leq 0.01$.

Table A5. Pearson's Correlation Analysis between SOC and remote sensing indices.

Variable	Correlation Coefficient	*p* Value	Variable	Correlation Coefficient	*p* Value
A–W	−0.201 **	0.00	b1–W	−0.242 **	0.00
A-S	0.112 **	0.01	b2–W	−0.262 **	0.00
B-S	0.114 **	0.00	b3–W	−0.185 **	0.00
B–W	−0.190 **	0.00	b4–W	−0.217 **	0.00
C-S	−0.106 **	0.01	b5–W	−0.232 **	0.00
C–W	0.01	0.80	b6–W	−0.08	0.05
D-S	−0.101 *	0.01	b7–W	−0.372 **	0.00
D–W	0.182 **	0.00	Far-S	0.141 **	0.00
E-S	0.05	0.27	Far–W	0.07	0.07
E–W	−0.253 **	0.00	Lai-S	0.144 **	0.00
b1-S	–0.03	0.39	Lai–W	0.082 *	0.04
b2-S	0.084 *	0.04	BLUE–W	−0.083 *	0.04
b3-S	0.06	0.15	MIR–W	−0.120 **	0.00
b4-S	0.02	0.64	NIR–W	−0.162 **	0.00
b5-S	0.08	0.06	RED–W	−0.150 **	0.00
b6-S	−0.07	0.11			
b7-S	−0.085 *	0.03			

Note: * $p \leq 0.05$; ** $p \leq 0.01$.

References

1. LeCain, D.R.; Morgan, J.A.; Schuman, G.E.; Reeder, J.D.; Hart, R.H. Carbon Exchange and Species Composition of Grazed Pastures and Exclosures in the Shortgrass Steppe of Colorado. *Agric. Ecosyst. Environ.* **2002**, *93*, 421–435. [CrossRef]
2. Wang, W.; Fang, J. Soil Respiration and Human Effects on Global Grasslands. *Glob. Planet. Change* **2009**, *67*, 20–28. [CrossRef]
3. Reeder, J.D.; Schuman, G.E. Influence of Livestock Grazing on C Sequestration in Semi-Arid Mixed-Grass and Short-Grass Rangelands. *Environ. Pollut.* **2002**, *116*, 457–463. [CrossRef]
4. Bagchi, S.; Ritchie, M.E. Introduced Grazers Can Restrict Potential Soil Carbon Sequestration through Impacts on Plant Community Composition: Soil Carbon and Livestock Production. *Ecol. Lett.* **2010**, *13*, 959–968. [CrossRef]
5. Jenkinson, D.S.; Adams, D.E.; Wild, A. Model Estimates of CO_2 Emissions from Soil in Response to Global Warming. *Nature* **1991**, *351*, 304–306. [CrossRef]
6. Lal, R. Soil Carbon Sequestration Impacts on Global Climate Change and Food Security. *Science* **2004**, *304*, 1623–1627. [CrossRef]
7. Scharlemann, J.P.; Tanner, E.V.; Hiederer, R.; Kapos, V. Global Soil Carbon: Understanding and Managing the Largest Terrestrial Carbon Pool. *Carbon Manag.* **2014**, *5*, 81–91. [CrossRef]
8. Qiao, Y.; Duan, Z. Understanding Alpine Meadow Ecosystems. In *Landscape and Ecosystem Diversity, Dynamics and Management in the Yellow River Source Zone*; Brierley, G.J., Li, X., Cullum, C., Gao, J., Eds.; Springer Geography; Springer International Publishing: Cham, Switzerland, 2016; pp. 117–135. ISBN 978-3-319-30473-1.
9. Wei, P.; Chen, S.; Wu, M.; Jia, Y.; Xu, H.; Liu, D. Increased Ecosystem Carbon Storage between 2001 and 2019 in the Northeastern Margin of the Qinghai-Tibet Plateau. *Remote Sens.* **2021**, *13*, 3986. [CrossRef]
10. Ghosh, P.; Mahanta, S. Carbon Sequestration in Grassland Systems. *Range Manag. Agrofor.* **2014**, *35*, 173–181.
11. Nicoll, T.; Brierley, G.; Yu, G. A Broad Overview of Landscape Diversity of the Yellow River Source Zone. *J. Geogr. Sci.* **2013**, *23*, 793–816. [CrossRef]
12. Blue, B.; Brierley, G.; Yu, G. Geodiversity in the Yellow River Source Zone. *J. Geogr. Sci.* **2013**, *23*, 775–792. [CrossRef]
13. Zhang, K.; Wang, X.; Wu, L.; Lu, T.; Guo, Y.; Ding, X. Impacts of Salinity on the Stability of Soil Organic Carbon in the Croplands of the Yellow River Delta. *Land Degrad. Dev.* **2021**, *32*, 1873–1882. [CrossRef]

14. Gao, B.; Li, J.; Wang, X. Impact of Frozen Soil Changes on Vegetation Phenology in the Source Region of the Yellow River from 2003 to 2015. *Theor. Appl. Climatol.* **2020**, *141*, 1219–1234. [CrossRef]
15. Yang, M.; Li, S.; Wang, S.; Huang, Q.; Shen, Q.; Kang, Y.; Shi, M.; Zhang, Y.; Luo, D. Latitudinal Gradient and Environmental Drivers of Soil Organic Carbon in Permafrost Regions of the Headwater Area of the Yellow River. *Carb Neutrality* **2025**, *4*, 16. [CrossRef]
16. Minasny, B.; McBratney, A.B. Digital Soil Mapping: A Brief History and Some Lessons. *Geoderma* **2016**, *264*, 301–311. [CrossRef]
17. Pouladi, N.; Møller, A.B.; Tabatabai, S.; Greve, M.H. Mapping Soil Organic Matter Contents at Field Level with Cubist, Random Forest and Kriging. *Geoderma* **2019**, *342*, 85–92. [CrossRef]
18. Wadoux, A.M.J.-C.; Minasny, B.; McBratney, A.B. Machine Learning for Digital Soil Mapping: Applications, Challenges and Suggested Solutions. *Earth-Sci. Rev.* **2020**, *210*, 103359. [CrossRef]
19. Yang, R.-M.; Zhang, G.-L.; Liu, F.; Lu, Y.-Y.; Yang, F.; Yang, F.; Yang, M.; Zhao, Y.-G.; Li, D.-C. Comparison of Boosted Regression Tree and Random Forest Models for Mapping Topsoil Organic Carbon Concentration in an Alpine Ecosystem. *Ecol. Indic.* **2016**, *60*, 870–878. [CrossRef]
20. Were, K.; Bui, D.T.; Dick, Ø.B.; Singh, B.R. A Comparative Assessment of Support Vector Regression, Artificial Neural Networks, and Random Forests for Predicting and Mapping Soil Organic Carbon Stocks across an Afromontane Landscape. *Ecol. Indic.* **2015**, *52*, 394–403. [CrossRef]
21. Kumar, S.; Lal, R.; Liu, D. A Geographically Weighted Regression Kriging Approach for Mapping Soil Organic Carbon Stock. *Geoderma* **2012**, *189*, 627–634. [CrossRef]
22. Ballabio, C.; Panagos, P.; Montanarella, L. Predicting Soil Organic Carbon Content in Cyprus Using Remote Sensing and Earth Observation Data. In Proceedings of the Second International Conference on Remote Sensing and Geoinformation of the Environment (RSCy2014), Paphos, Cyprus, 7–10 April 2014; Hadjimitsis, D.G., Themistocleous, K., Michaelides, S., Papadavid, G., Eds.; SPIE: Bellingham, WA, USA, 2014; Volume 9229, pp. 96–104.
23. Ye, Z.; Sheng, Z.; Liu, X.; Ma, Y.; Wang, R.; Ding, S.; Liu, M.; Li, Z.; Wang, Q. Using Machine Learning Algorithms Based on GF-6 and Google Earth Engine to Predict and Map the Spatial Distribution of Soil Organic Matter Content. *Sustainability* **2021**, *13*, 14055. [CrossRef]
24. Tziachris, P.; Aschonitis, V.; Chatzistathis, T.; Papadopoulou, M. Assessment of Spatial Hybrid Methods for Predicting Soil Organic Matter Using DEM Derivatives and Soil Parameters. *CATENA* **2019**, *174*, 206–216. [CrossRef]
25. Krull, E.S.; Baldock, J.A.; Skjemstad, J.O. Importance of Mechanisms and Processes of the Stabilisation of Soil Organic Matter for Modelling Carbon Turnover. *Funct. Plant Biol.* **2003**, *30*, 207–222. [CrossRef]
26. Yang, L.-X.; Pan, J.-J. Dynamics Models of Soil Organic Carbon. *J. For. Res.* **2003**, *14*, 323–330. [CrossRef]
27. Jin, Z.; Ping, L.; Wong, M. Systematic Relationship between Soil Properties and Organic Carbon Mineralization Based on Structural Equation Modeling Analysis. *J. Clean. Prod.* **2020**, *277*, 123338. [CrossRef]
28. Piao, S.; Fang, J.; Ciais, P.; Peylin, P.; Huang, Y.; Sitch, S.; Wang, T. The Carbon Balance of Terrestrial Ecosystems in China. *Nature* **2009**, *458*, 1009–1013. [CrossRef] [PubMed]
29. Batlle-Aguilar, J.; Brovelli, A.; Porporato, A.; Barry, D.A. Modelling Soil Carbon and Nitrogen Cycles during Land Use Change. In *Sustainable Agriculture Volume 2*; Lichtfouse, E., Hamelin, M., Navarrete, M., Debaeke, P., Eds.; Springer: Dordrecht, The Netherlands, 2011; pp. 499–527. ISBN 978-94-007-0393-3.
30. Stockmann, U.; Adams, M.A.; Crawford, J.W.; Field, D.J.; Henakaarchchi, N.; Jenkins, M.; Minasny, B.; McBratney, A.B.; Courcelles, V.D.R.D.; Singh, K.; et al. The Knowns, Known Unknowns and Unknowns of Sequestration of Soil Organic Carbon. *Agric. Ecosyst. Environ.* **2013**, *164*, 80–99. [CrossRef]
31. Dwivedi, R.S. Soil Resources Mapping: A Remote Sensing Perspective. *Remote Sens. Rev.* **2001**, *20*, 89–122. [CrossRef]
32. Knox, N.M.; Grunwald, S.; McDowell, M.L.; Bruland, G.L.; Myers, D.B.; Harris, W.G. Modelling Soil Carbon Fractions with Visible Near-Infrared (VNIR) and Mid-Infrared (MIR) Spectroscopy. *Geoderma* **2015**, *239–240*, 229–239. [CrossRef]
33. Post, W.; King, A.; Wullschleger, S. Soil Organic Matter Models and Global Estimates of Soil Organic Carbon. In *Evaluation of Soil Organic Matter Models: Using Existing Long-Term Datasets*; Springer: Berlin/Heidelberg, Germany, 1996; pp. 201–222.
34. Yang, R.-M.; Huang, L.-M.; Zhang, X.; Zhu, C.-M.; Xu, L. Mapping the Distribution, Trends, and Drivers of Soil Organic Carbon in China from 1982 to 2019. *Geoderma* **2023**, *429*, 116232. [CrossRef]
35. Yang, C.; Shen, F.; Li, X.; Cui, W.; Zhang, L.; Yang, L.; Zhou, C. Spatio-Temporal Mapping Reveals Changes in Soil Organic Carbon Stocks across the Contiguous United States since 1955. *Commun. Earth Environ.* **2025**, *6*, 615. [CrossRef]
36. Dorji, T.; Odeh, I.O.; Field, D.J.; Baillie, I.C. Digital Soil Mapping of Soil Organic Carbon Stocks under Different Land Use and Land Cover Types in Montane Ecosystems, Eastern Himalayas. *For. Ecol. Manag.* **2014**, *318*, 91–102. [CrossRef]
37. Adhikari, K.; Hartemink, A.E.; Minasny, B.; Bou Kheir, R.; Greve, M.B.; Greve, M.H. Digital Mapping of Soil Organic Carbon Contents and Stocks in Denmark. *PLoS ONE* **2014**, *9*, e105519. [CrossRef]
38. Taghizadeh-Mehrjardi, R.; Nabiollahi, K.; Kerry, R. Digital Mapping of Soil Organic Carbon at Multiple Depths Using Different Data Mining Techniques in Baneh Region, Iran. *Geoderma* **2016**, *266*, 98–110. [CrossRef]

39. Sreenivas, K.; Dadhwal, V.; Kumar, S.; Harsha, G.S.; Mitran, T.; Sujatha, G.; Suresh, G.J.R.; Fyzee, M.; Ravisankar, T. Digital Mapping of Soil Organic and Inorganic Carbon Status in India. *Geoderma* **2016**, *269*, 160–173. [CrossRef]
40. Park, S.-J.; Kwon, S.-I.; Kim, S.-H.; Shim, J.; Lee, Y.-H.; Oh, T.-K. Estimation of Soil Organic Carbon (SOC) Stock in South Korea Using Digital Soil Mapping Technique. *Korean J. Soil Sci. Fertil.* **2021**, *54*, 247–256. [CrossRef]
41. Ratnayake, R.; Karunaratne, S.; Lessels, J.; Yogenthiran, N.; Rajapaksha, R.; Gnanavelrajah, N. Digital Soil Mapping of Organic Carbon Concentration in Paddy Growing Soils of Northern Sri Lanka. *Geoderma Reg.* **2016**, *7*, 167–176. [CrossRef]
42. Grimm, R.; Behrens, T.; Märker, M.; Elsenbeer, H. Soil Organic Carbon Concentrations and Stocks on Barro Colorado Island—Digital Soil Mapping Using Random Forests Analysis. *Geoderma* **2008**, *146*, 102–113. [CrossRef]
43. Siewert, M.B. High-Resolution Digital Mapping of Soil Organic Carbon in Permafrost Terrain Using Machine Learning: A Case Study in a Sub-Arctic Peatland Environment. *Biogeosciences* **2018**, *15*, 1663–1682. [CrossRef]
44. Zhu, M.; Feng, Q.; Zhang, M.; Liu, W.; Qin, Y.; Deo, R.C.; Zhang, C. Effects of Topography on Soil Organic Carbon Stocks in Grasslands of a Semiarid Alpine Region, Northwestern China. *J. Soils Sediments* **2019**, *19*, 1640–1650. [CrossRef]
45. Martin, M.P.; Wattenbach, M.; Smith, P.; Meersmans, J.; Jolivet, C.; Boulonne, L.; Arrouays, D. Spatial Distribution of Soil Organic Carbon Stocks in France. *Biogeosciences* **2011**, *8*, 1053–1065. [CrossRef]
46. Bhunia, G.S.; Shit, P.K.; Maiti, R. Comparison of GIS-Based Interpolation Methods for Spatial Distribution of Soil Organic Carbon (SOC). *J. Saudi Soc. Agric. Sci.* **2018**, *17*, 114–126. [CrossRef]
47. Yang, X.; Bai, X.; Yao, W.; Li, P.; Hu, J.; Kang, L. Spatioemporal Dynamics and Driving Forces of Soil Organic Carbon Changes in an Arid Coal Mining Area of China Investigated Based on Remote Sensing Techniques. *Ecol. Indic.* **2024**, *158*, 111453. [CrossRef]
48. Liu, B.; Qian, J.; Zhao, R.; Yang, Q.; Wu, K.; Zhao, H.; Feng, Z.; Dong, J. Spatio-Temporal Variation and Its Driving Forces of Soil Organic Carbon along an Urban–Rural Gradient: A Case Study of Beijing. *Int. J. Environ. Res. Public Health* **2022**, *19*, 15201. [CrossRef] [PubMed]
49. Geremew, B.; Tadesse, T.; Bedadi, B.; Gollany, H.T.; Tesfaye, K.; Aschalew, A. Impact of Land Use/Cover Change and Slope Gradient on Soil Organic Carbon Stock in Anjeni Watershed, Northwest Ethiopia. *Environ. Monit. Assess.* **2023**, *195*, 971. [CrossRef]
50. Hao, X.; Yang, J.; Dong, S.; He, F.; Zhang, Y. The Influence of Grazing Intensity on Soil Organic Carbon Storage in Grassland of China: A Meta-Analysis. *Sci. Total Environ.* **2024**, *924*, 171439. [CrossRef]
51. Shen, Y.; Fang, Y.; Chen, H.; Ma, Z.; Huang, C.; Wu, X.; Chang, S.X.; Tavakkoli, E.; Cai, Y. New Insights into the Relationships between Livestock Grazing Behaviors and Soil Organic Carbon Stock in an Alpine Grassland. *Agric. Ecosyst. Environ.* **2023**, *355*, 108602. [CrossRef]
52. Wang, J.; Li, W.; Cao, W.; Wang, S. Effects of Different Intensities of Long-Term Grazing on Plant Diversity, Biomass and Carbon Stock in Alpine Shrubland on the Qinghai-Tibetan Plateau. *PeerJ* **2022**, *10*, e12771. [CrossRef]
53. Jones, C.; McConnell, C.; Coleman, K.; Cox, P.; Falloon, P.; Jenkinson, D.; Powlson, D. Global Climate Change and Soil Carbon Stocks; Predictions from Two Contrasting Models for the Turnover of Organic Carbon in Soil. *Glob. Change Biol.* **2005**, *11*, 154–166. [CrossRef]
54. Qi, R.; Li, J.; Lin, Z.; Li, Z.; Li, Y.; Yang, X.; Zhang, J.; Zhao, B. Temperature Effects on Soil Organic Carbon, Soil Labile Organic Carbon Fractions, and Soil Enzyme Activities under Long-Term Fertilization Regimes. *Appl. Soil Ecol.* **2016**, *102*, 36–45. [CrossRef]
55. Wang, H.; Wu, J.; Li, G.; Yan, L.; Liu, S. Effects of Extreme Rainfall Frequency on Soil Organic Carbon Fractions and Carbon Pool in a Wet Meadow on the Qinghai-Tibet Plateau. *Ecol. Indic.* **2023**, *146*, 109853. [CrossRef]
56. Zhu, M.; Feng, Q.; Qin, Y.; Cao, J.; Zhang, M.; Liu, W.; Deo, R.C.; Zhang, C.; Li, R.; Li, B. The Role of Topography in Shaping the Spatial Patterns of Soil Organic Carbon. *Catena* **2019**, *176*, 296–305. [CrossRef]
57. Bangroo, S.; Najar, G.; Rasool, A. Effect of Altitude and Aspect on Soil Organic Carbon and Nitrogen Stocks in the Himalayan Mawer Forest Range. *Catena* **2017**, *158*, 63–68. [CrossRef]
58. Zhang, J.; Lan, Z.; Li, H.; Jaffar, M.T.; Li, X.; Cui, L.; Han, J. Coupling Effects of Soil Organic Carbon and Moisture under Different Land Use Types, Seasons and Slope Positions in the Loess Plateau. *Catena* **2023**, *233*, 107520. [CrossRef]
59. Błońska, E.; Lasota, J. Soil Organic Matter Accumulation and Carbon Fractions along a Moisture Gradient of Forest Soils. *Forests* **2017**, *8*, 448. [CrossRef]
60. Tang, K.; Li, F.Y.; Jaesong, S.; Liu, Y.; Sun, T.; Liu, J.; Gao, X.; Wang, Y. Soil Water Retention Capacity Surpasses Climate Humidity in Determining Soil Organic Carbon Content but Not Plant Production in the Steppe Zone of Northern China. *Ecol. Indic.* **2022**, *141*, 109129. [CrossRef]
61. Zhang, Y.; Zhang, G.; Pan, J.; Fan, Z.; Chen, F.; Liu, Y. Soil Organic Carbon Distribution in Relation to Terrain & Land Use—A Case Study in a Small Watershed of Danjiangkou Reservoir Area, China. *Glob. Ecol. Conserv.* **2019**, *20*, e00731. [CrossRef]
62. Ma, H.; Peng, M.; Yang, Z.; Yang, K.; Zhao, C.; Li, K.; Guo, F.; Yang, Z.; Cheng, H. Spatial Distribution and Driving Factors of Soil Organic Carbon in the Northeast China Plain: Insights from Latest Monitoring Data. *Sci. Total Environ.* **2024**, *911*, 168602. [CrossRef]

63. Wu, Y.; Liu, S.; Tan, Z. Quantitative Attribution of Major Driving Forces on Soil Organic Carbon Dynamics. *J. Adv. Model. Earth Syst.* **2015**, *7*, 21–34. [CrossRef]
64. Ahirwal, J.; Nath, A.; Brahma, B.; Deb, S.; Sahoo, U.K.; Nath, A.J. Patterns and Driving Factors of Biomass Carbon and Soil Organic Carbon Stock in the Indian Himalayan Region. *Sci. Total Environ.* **2021**, *770*, 145292. [CrossRef] [PubMed]
65. Hamzehpour, N.; Shafizadeh-Moghadam, H.; Valavi, R. Exploring the Driving Forces and Digital Mapping of Soil Organic Carbon Using Remote Sensing and Soil Texture. *Catena* **2019**, *182*, 104141. [CrossRef]
66. Han, L.; Sun, K.; Jin, J.; Xing, B. Some Concepts of Soil Organic Carbon Characteristics and Mineral Interaction from a Review of Literature. *Soil Biol. Biochem.* **2016**, *94*, 107–121. [CrossRef]
67. Jungkunst, H.F.; Göpel, J.; Horvath, T.; Ott, S.; Brunn, M. Global Soil Organic Carbon–Climate Interactions: Why Scales Matter. *Wiley Interdiscip. Rev. Clim. Change* **2022**, *13*, e780. [CrossRef]
68. Yu, K.; Yang, C.; Wu, T.; Zhai, Y.; Tian, S.; Feng, Y. Analysis of Vegetation Coverage Changes and Driving Forces in the Source Region of the Yellow River. *Sci. Rep.* **2025**, *15*, 22569. [CrossRef]
69. Wang, Y.; Wang, X.; Li, C.; Wu, F.; Yang, Z. Spatiotemporal Analysis of Temperature Trends under Climate Change in the Source Region of the Yellow River, China. *Theor. Appl. Climatol.* **2015**, *119*, 123–133. [CrossRef]
70. Yuan, F.; Berndtsson, R.; Zhang, L.; Uvo, C.B.; Hao, Z.; Wang, X.; Yasuda, H. Hydro Climatic Trend and Periodicity for the Source Region of the Yellow River. *J. Hydrol. Eng.* **2015**, *20*, 05015003. [CrossRef]
71. Lin, H.; Zhao, Y. Soil Erosion Assessment of Alpine Grassland in the Source Park of the Yellow River on the Qinghai-Tibetan Plateau, China. *Front. Ecol. Evol.* **2022**, *9*, 771439. [CrossRef]
72. Fu, J.-T.; Hu, X.-S.; Li, X.-L.; Zhao, J.-M.; Xing, G.-Y.; Liu, C.-Y. Impact of Meadow Degradations on the Probabilistic Distribution Patterns of Physical and Mechanical Indices of Rooted Soil in the Upper Regions of the Yellow River, China. *Water* **2024**, *16*, 1205. [CrossRef]
73. Ling, W. Three-River-Source National Park System Pilot Area's Steps toward Cohesive Conservation and Management. *Int. J. Geoheritage Parks* **2020**, *8*, 220–224. [CrossRef]
74. Liang, T.; Feng, Q.; Huang, X.; Ren, J. Review in the Study of Comprehensive Sequential Classification System of Grassland. *Acta Prataculturae Sinica* **2011**, *20*, 252–258, (In Chinese with English abstract).
75. Worsham, L.; Markewitz, D.; Nibbelink, N.P.; West, L.T. A Comparison of Three Field Sampling Methods to Estimate Soil Carbon Content. *For. Sci.* **2012**, *58*, 513–522. [CrossRef]
76. Minasny, B.; McBratney, A.B. A Conditioned Latin Hypercube Method for Sampling in the Presence of Ancillary Information. *Comput. Geosci.* **2006**, *32*, 1378–1388. [CrossRef]
77. Yang, L.; Li, X.; Shi, J.; Shen, F.; Qi, F.; Gao, B.; Chen, Z.; Zhu, A.-X.; Zhou, C. Evaluation of Conditioned Latin Hypercube Sampling for Soil Mapping Based on a Machine Learning Method. *Geoderma* **2020**, *369*, 114337. [CrossRef]
78. Gerenfes, D.; Giorgis, A.; Negasa, G. Comparison of Organic Matter Determination Methods in Soil by Loss on Ignition and Potassium Dichromate Method. *Int. J. Hortic. Food Sci.* **2022**, *4*, 49–53. [CrossRef]
79. Ciavatta, C.; Antisari, L.V.; Sequi, P. Determination of Organic Carbon in Soils and Fertilizers. *Commun. Soil Sci. Plant Anal.* **1989**, *20*, 759–773. [CrossRef]
80. Vélez, S.; Martínez-Peña, R.; Castrillo, D. Beyond Vegetation: A Review Unveiling Additional Insights into Agriculture and Forestry through the Application of Vegetation Indices. *J* **2023**, *6*, 421–436. [CrossRef]
81. Zhong, S.; Sun, Z.; Di, L. Characteristics of Vegetation Response to Drought in the CONUS Based on Long-Term Remote Sensing and Meteorological Data. *Ecol. Indic.* **2021**, *127*, 107767. [CrossRef]
82. Xue, J.; Su, B. Significant Remote Sensing Vegetation Indices: A Review of Developments and Applications. *J. Sens.* **2017**, *2017*, 1353691. [CrossRef]
83. Shangguan, W.; Dai, Y. *A China Soil Characteristics Dataset (2010)*; National Tibetan Plateau Data Center: Beijing, China, 2019.
84. Shi, G.; Sun, W. *A China Dataset of Soil Properties for Land Surface Modeling (Version 2, CSDLv2)*; National Tibetan Plateau Data Center: Beijing, China, 2025.
85. Wilkinson, L. Tests of Significance in Stepwise Regression. *Psychol. Bull.* **1979**, *86*, 168. [CrossRef]
86. Efroymson, M. *Stepwise Regression—A Backward and Forward Look*; Eastern Regional Meetings of the Institute of Mathematical Statistics: Florham Park, NJ, USA, 1966; pp. 27–29.
87. Hastie, T. Ridge Regularization: An Essential Concept in Data Science. *Technometrics* **2020**, *62*, 426–433. [CrossRef]
88. Warton, D.I. Penalized Normal Likelihood and Ridge Regularization of Correlation and Covariance Matrices. *J. Am. Stat. Assoc.* **2008**, *103*, 340–349. [CrossRef]
89. Tibshirani, R. Regression Shrinkage and Selection via the Lasso. *J. R. Stat. Soc. Ser. B (Methodol.)* **1996**, *58*, 267–288. [CrossRef]
90. Ranstam, J.; Cook, J.A. LASSO Regression. *J. Br. Surg.* **2018**, *105*, 1348. [CrossRef]
91. Abdi, H. Partial Least Squares Regression and Projection on Latent Structure Regression (PLS Regression). *Wiley Interdiscip. Rev. Comput. Stat.* **2010**, *2*, 97–106. [CrossRef]
92. Abdi, H. Partial Least Square Regression (PLS Regression). *Encycl. Res. Methods Soc. Sci.* **2003**, *6*, 792–795.

93. Breiman, L. Random Forests. *Mach. Learn.* **2001**, *45*, 5–32. [CrossRef]
94. Rigatti, S.J. Random Forest. *J. Insur. Med.* **2017**, *47*, 31–39. [CrossRef]
95. Burges, C.J. A Tutorial on Support Vector Machines for Pattern Recognition. *Data Min. Knowl. Discov.* **1998**, *2*, 121–167. [CrossRef]
96. Jakkula, V. *Tutorial on Support Vector Machine (Svm)*; School of EECS, Washington State University: Pullman, WA, USA, 2006; pp. 1–13.
97. Ke, G.; Meng, Q.; Finley, T.; Wang, T.; Chen, W.; Ma, W.; Ye, Q.; Liu, T.-Y. Lightgbm: A Highly Efficient Gradient Boosting Decision Tree. *Adv. Neural Inf. Process. Syst.* **2017**, *30*, 3149–3157.
98. Mann, H.B. Nonparametric Tests against Trend. *Econometrica* **1945**, *13*, 245–259. [CrossRef]
99. Kendall, M.G. *Rank Correlation Methods*; Charles Griffin & Company: London, UK, 1948.
100. Wang, J.-F.; Li, X.-H.; Christakos, G.; Liao, Y.-L.; Zhang, T.; Gu, X.; Zheng, X.-Y. Geographical Detectors-Based Health Risk Assessment and Its Application in the Neural Tube Defects Study of the Heshun Region, China. *Int. J. Geogr. Inf. Sci.* **2010**, *24*, 107–127. [CrossRef]
101. Stern, N.H. *The Economics of Climate Change: The Stern Review*; Cambridge University Press: Cambridge, UK, 2007.
102. Nordhaus, W. A Review of the Stern Review on the Economics of Global Warming. *J. Econ. Lit.* **2007**, *45*, 686–702. [CrossRef]
103. Tol, R.S. The Marginal Damage Costs of Carbon Dioxide Emissions: An Assessment of the Uncertainties. *Energy Policy* **2005**, *33*, 2064–2074. [CrossRef]
104. Ahmed, M.P.; Arif, M.; Al Mamun, A.; Mahmud, F.; Rahman, T.; Ahmmed, M.J.; Mou, S.N.; Akter, P.; Chowdhury, M.S.R.; Uddin, M.K. A Comparative Study of Machine Learning Models for Predicting Customer Churn in Retail Banking: Insights from Logistic Regression, Random Forest, GBM, and SVM. *J. Comput. Sci. Technol. Stud.* **2024**, *6*, 92–101. [CrossRef]
105. Xi, B.; Li, E.; Fissha, Y.; Zhou, J.; Segarra, P. LGBM-Based Modeling Scenarios to Compressive Strength of Recycled Aggregate Concrete with SHAP Analysis. *Mech. Adv. Mater. Struct.* **2024**, *31*, 5999–6014. [CrossRef]
106. Sibindi, R.; Mwangi, R.W.; Waititu, A.G. A Boosting Ensemble Learning Based Hybrid Light Gradient Boosting Machine and Extreme Gradient Boosting Model for Predicting House Prices. *Eng. Rep.* **2023**, *5*, e12599. [CrossRef]
107. Effrosynidis, D.; Arampatzis, A. An Evaluation of Feature Selection Methods for Environmental Data. *Ecol. Inform.* **2021**, *61*, 101224. [CrossRef]
108. Muthukrishnan, R.; Rohini, R. LASSO: A Feature Selection Technique in Predictive Modeling for Machine Learning. In Proceedings of the 2016 IEEE International Conference on Advances in Computer Applications (ICACA), Coimbatore, India, 24 October 2016; IEEE: New York, NY, USA, 2016; pp. 18–20.
109. Pak, A.; Rad, A.K.; Nematollahi, M.J.; Mahmoudi, M. Application of the Lasso Regularisation Technique in Mitigating Overfitting in Air Quality Prediction Models. *Sci. Rep.* **2025**, *15*, 547. [CrossRef] [PubMed]
110. Li, L.; Liang, W.; Awada, T.; Hiller, J.; Kaiser, M. Machine Learning for Modeling Soil Organic Carbon as Affected by Land Cover Change in the Nebraska Sandhills, USA. *Environ. Model. Assess.* **2024**, *29*, 535–547. [CrossRef]
111. Liu, Y.; Wu, X.; Wu, T.; Zhao, L.; Li, R.; Li, W.; Hu, G.; Zou, D.; Ni, J.; Du, Y.; et al. Soil Texture and Its Relationship with Environmental Factors on the Qinghai–Tibet Plateau. *Remote Sens.* **2022**, *14*, 3797. [CrossRef]
112. Liu, Y.; Ni, Z.; Zhao, Y.; Zhou, G.; Luo, Y.; Li, S.; Wang, D.; Zhang, S. Spatial-Temporal Evolution and Driving Forces of Drying Trends on the Qinghai-Tibet Plateau Based on Geomorphological Division. *Int. J. Environ. Res. Public Health* **2022**, *19*, 7909. [CrossRef] [PubMed]
113. Xin, Z.; Qin, Y.; Yu, X. Spatial Variability in Soil Organic Carbon and Its Influencing Factors in a Hilly Watershed of the Loess Plateau, China. *Catena* **2016**, *137*, 660–669. [CrossRef]
114. Luo, Z.; Feng, W.; Luo, Y.; Baldock, J.; Wang, E. Soil Organic Carbon Dynamics Jointly Controlled by Climate, Carbon Inputs, Soil Properties and Soil Carbon Fractions. *Glob. Change Biol.* **2017**, *23*, 4430–4439. [CrossRef] [PubMed]
115. Canero, F.M.; Rodriguez-Galiano, V.; Aragones, D. Machine Learning and Feature Selection for Soil Spectroscopy. An Evaluation of Random Forest Wrappers to Predict Soil Organic Matter, Clay, and Carbonates. *Heliyon* **2024**, *10*, e30228. [CrossRef]
116. Taghizadeh-Mehrjardi, R.; Schmidt, K.; Amirian-Chakan, A.; Rentschler, T.; Zeraatpisheh, M.; Sarmadian, F.; Valavi, R.; Davatgar, N.; Behrens, T.; Scholten, T. Improving the Spatial Prediction of Soil Organic Carbon Content in Two Contrasting Climatic Regions by Stacking Machine Learning Models and Rescanning Covariate Space. *Remote Sens.* **2020**, *12*, 1095. [CrossRef]
117. Cao, Z.; Wang, Y.; Li, J.; Zhang, J.; He, N. Soil Organic Carbon Contents, Aggregate Stability, and Humic Acid Composition in Different Alpine Grasslands in Qinghai-Tibet Plateau. *J. Mt. Sci.* **2016**, *13*, 2015–2027. [CrossRef]
118. Liu, S.; Sun, Y.; Dong, Y.; Zhao, H.; Dong, S.; Zhao, S.; Beazley, R. The Spatio-Temporal Patterns of the Topsoil Organic Carbon Density and Its Influencing Factors Based on Different Estimation Models in the Grassland of Qinghai-Tibet Plateau. *PLoS ONE* **2019**, *14*, e0225952. [CrossRef]
119. Kirschbaum, M.U.F. Will Changes in Soil Organic Carbon Act as a Positive or Negative Feedback on Global Warming? *Biogeochemistry* **2000**, *48*, 21–51. [CrossRef]
120. Tian, Q.; Yang, F.; Wang, Z.; Zhang, Q. Variation of Soil Organic Carbon Components and Enzyme Activities during the Ecological Restoration in a Temperate Forest. *Ecol. Eng.* **2024**, *201*, 107192. [CrossRef]

121. Gurmu, G. Soil Organic Matter and Its Role in Soil Health and Crop Productivity Improvement. *For. Ecol. Manag.* **2019**, *7*, 475–483.
122. Li, W.; Xia, Y.; Tan, X.; Gan, F.; Jiang, L.; Xu, X.; Yan, Y.; Fan, Y.; Pu, J. Does the Returning Farmland to Grassland (Retiring Grassland) Improve the Soil Aggregate Stability in Erosion and Deposition Sites? *Catena* **2025**, *255*, 109023. [CrossRef]
123. Shi, S.; Wang, P.; Zhan, X.; Han, J.; Guo, M.; Wang, F. Warming and Increasing Precipitation Induced Greening on the Northern Qinghai-Tibet Plateau. *Catena* **2023**, *233*, 107483. [CrossRef]
124. Li, L.; Yang, S.; Wang, Z.; Zhu, X.; Tang, H. Evidence of Warming and Wetting Climate over the Qinghai-Tibet Plateau. *Arct. Antarct. Alp. Res.* **2010**, *42*, 449–457. [CrossRef]
125. Huang, K.; Zhang, Y.; Zhu, J.; Liu, Y.; Zu, J.; Zhang, J. The Influences of Climate Change and Human Activities on Vegetation Dynamics in the Qinghai-Tibet Plateau. *Remote Sens.* **2016**, *8*, 876. [CrossRef]
126. Zhou, W.; Wang, T.; Xiao, J.; Wang, K.; Yu, W.; Du, Z.; Huang, L.; Yue, T. Grassland Productivity Increase Was Dominated by Climate in Qinghai-Tibet Plateau from 1982 to 2020. *J. Clean. Prod.* **2024**, *434*, 140144. [CrossRef]
127. Chen, B.; Zhang, X.; Tao, J.; Wu, J.; Wang, J.; Shi, P.; Zhang, Y.; Yu, C. The Impact of Climate Change and Anthropogenic Activities on Alpine Grassland over the Qinghai-Tibet Plateau. *Agric. For. Meteorol.* **2014**, *189*, 11–18. [CrossRef]
128. Liu, S.; Du, Y.; Zhang, F.; Lin, L.; Li, Y.; Guo, X.; Li, Q.; Cao, G. Distribution of Soil Carbon in Different Grassland Types of the Qinghai-Tibetan Plateau. *J. Mt. Sci.* **2016**, *13*, 1806–1817. [CrossRef]
129. Nie, X.; Wang, D.; Ren, L.; Du, Y.; Zhou, G. Storage and Controlling Factors of Soil Organic Carbon in Alpine Wetlands and Meadow across the Tibetan Plateau. *Eur. J. Soil Sci.* **2023**, *74*, e13383. [CrossRef]
130. Wang, H.; Wu, J.; Li, G.; Yan, L.; Wei, X. Effects of Rainfall Frequency on Soil Labile Carbon Fractions in a Wet Meadow on the Qinghai-Tibet Plateau. *J. Soils Sediments* **2022**, *22*, 1489–1499. [CrossRef]
131. Alhassan, A.-R.M.; Ma, W.; Li, G.; Jiang, Z.; Wu, J.; Chen, G. Response of Soil Organic Carbon to Vegetation Degradation along a Moisture Gradient in a Wet Meadow on the Qinghai–Tibet Plateau. *Ecol. Evol.* **2018**, *8*, 11999–12010. [CrossRef]
132. Zhao, W.; Cheng, Y.; Jian, J.; Jiao, J.; Cheng, C.; Li, J.; Chen, T. Water Erosion Changes on the Qinghai-Tibet Plateau and Its Response to Climate Variability and Human Activities during 1982–2015. *Catena* **2023**, *229*, 107207. [CrossRef]
133. Wei, P.; Du, J.; Bahadur, A.; Zhang, H.; Wang, S.; Wu, T.; Chen, S. Soil Erosion and Risk Assessment on the Qinghai-Tibetan Plateau. *Commun. Earth Environ.* **2025**, *6*, 365. [CrossRef]
134. Wu, M.-H.; Chen, S.-Y.; Chen, J.-W.; Xue, K.; Chen, S.-L.; Wang, X.-M.; Chen, T.; Kang, S.-C.; Rui, J.-P.; Thies, J.E.; et al. Reduced Microbial Stability in the Active Layer Is Associated with Carbon Loss under Alpine Permafrost Degradation. *Proc. Natl. Acad. Sci. USA* **2021**, *118*, e2025321118. [CrossRef]
135. Chen, S.; Gu, Y.; Liu, E.; Wu, M.; Cheng, X.; Yang, P.; Bahadur, A.; Bai, R.; Chen, J.; Zhang, M.; et al. Freeze-Thaw Strength Increases Microbial Stability to Enhance Diversity-Soil Multifunctionality Relationship. *Commun. Earth Environ.* **2024**, *5*, 578. [CrossRef]
136. Kang, H.; Yu, W.; Dutta, S.; Gao, H. Soil Microbial Community Composition and Function Are Closely Associated with Soil Organic Matter Chemistry along a Latitudinal Gradient. *Geoderma* **2021**, *383*, 114744. [CrossRef]
137. Wang, J.; Song, C.; Wang, X.; Song, Y. Changes in Labile Soil Organic Carbon Fractions in Wetland Ecosystems along a Latitudinal Gradient in Northeast China. *Catena* **2012**, *96*, 83–89. [CrossRef]
138. Yin, S.; Wang, C.; Zhou, Z. Globally Altitudinal Trends in Soil Carbon and Nitrogen Storages. *Catena* **2022**, *210*, 105870. [CrossRef]
139. Buraka, T.; Elias, E.; Lelago, A. Soil Organic Carbon and Its' Stock Potential in Different Land-Use Types along Slope Position in Coka Watershed, Southern Ethiopia. *Heliyon* **2022**, *8*, e10261. [CrossRef]
140. Ritchie, J.C.; McCarty, G.W.; Venteris, E.R.; Kaspar, T. Soil and Soil Organic Carbon Redistribution on the Landscape. *Geomorphology* **2007**, *89*, 163–171. [CrossRef]
141. Leifeld, J.; Zimmermann, M.; Fuhrer, J. Simulating Decomposition of Labile Soil Organic Carbon: Effects of pH. *Soil Biol. Biochem.* **2008**, *40*, 2948–2951. [CrossRef]
142. Malik, A.A.; Puissant, J.; Buckeridge, K.M.; Goodall, T.; Jehmlich, N.; Chowdhury, S.; Gweon, H.S.; Peyton, J.M.; Mason, K.E.; van Agtmaal, M.; et al. Land Use Driven Change in Soil pH Affects Microbial Carbon Cycling Processes. *Nat. Commun.* **2018**, *9*, 3591. [CrossRef]
143. McCauley, A.; Jones, C.; Jacobsen, J. Soil pH and Organic Matter. *Nutr. Manag. Modul.* **2009**, *8*, 1–12.
144. Kuzyakov, Y. Priming Effects: Interactions between Living and Dead Organic Matter. *Soil Biol. Biochem.* **2010**, *42*, 1363–1371. [CrossRef]
145. Liang, C.; Balser, T.C. Microbial Production of Recalcitrant Organic Matter in Global Soils: Implications for Productivity and Climate Policy. *Nat. Rev. Microbiol.* **2011**, *9*, 75. [CrossRef] [PubMed]
146. Fontaine, S.; Barot, S.; Barré, P.; Bdioui, N.; Mary, B.; Rumpel, C. Stability of Organic Carbon in Deep Soil Layers Controlled by Fresh Carbon Supply. *Nature* **2007**, *450*, 277–280. [CrossRef] [PubMed]
147. Scholes, M.C.; Powlson, D.; Tian, G. Input Control of Organic Matter Dynamics. *Geoderma* **1997**, *79*, 25–47. [CrossRef]
148. Wang, Y.; Lv, W.; Xue, K.; Wang, S.; Zhang, L.; Hu, R.; Zeng, H.; Xu, X.; Li, Y.; Jiang, L.; et al. Grassland Changes and Adaptive Management on the Qinghai–Tibetan Plateau. *Nat. Rev. Earth Environ.* **2022**, *3*, 668–683. [CrossRef]

149. Harris, R.B. Rangeland Degradation on the Qinghai-Tibetan Plateau: A Review of the Evidence of Its Magnitude and Causes. *J. Arid Environ.* **2010**, *74*, 1–12. [CrossRef]
150. Sheehy, D.P.; Miller, D.; Johnson, D.A. Transformation of Traditional Pastoral Livestock Systems on the Tibetan Steppe. *Sci. Et Chang. Planétaires/Sécheresse* **2006**, *17*, 142–151.
151. Lu, T.; Li, C.; Wang, S.; Zhou, W.; Li, Y.; Mao, Z.; Tang, Q.; Liu, J.; Xu, J. Projected Humidification Expands the Sustainable Grazing Areas in the Drylands of the Qinghai–Xizang Plateau. *Ecosyst. Health Sustain.* **2024**, *10*, 0284. [CrossRef]
152. Yang, H.; Sun, Z.; Lu, Q.; Gao, W.; Bai, Y. Effects of Seasonal Rest Grazing on Soil Aggregate Stability and Organic Carbon in Alpine Grasslands in Northern Xizang. *Land Degrad. Dev.* **2025**, *36*, 3350–3365. [CrossRef]
153. Xiao, Z. Geographical Features of Agricultural Technology in the Qinghai-Xizang (Tibet) Plateau in the Qing Dynasty. In *Environment and Selection of Technology: The Historical Agrotechnical Geography of West China During the Qing Dynasty*; Springer: Berlin/Heidelberg, Germany, 2024; pp. 83–100.
154. Tomelleri, E. others Modeling the Carbon Cycle and Its Interactions with Management Practices in Grasslands. 2007. Available online: https://hdl.handle.net/11577/3426898 (accessed on 24 December 2025).
155. Duan, H.; Xue, X.; Wang, T.; Kang, W.; Liao, J.; Liu, S. Spatial and Temporal Differences in Alpine Meadow, Alpine Steppe and All Vegetation of the Qinghai-Tibetan Plateau and Their Responses to Climate Change. *Remote Sens.* **2021**, *13*, 669. [CrossRef]
156. Ward, A. The Extent and Value of Carbon Stored in Mountain Grasslands and Shrublands Globally, and the Prospects for Using Climate Finance to Address Natural Resource Management Issues. Ph.D. Thesis, The University of Queensland, Brisbane, Australia, 2016.
157. Liu, S.; Zhang, F.; Du, Y.; Guo, X.; Lin, L.; Li, Y.; Li, Q.; Cao, G. Ecosystem Carbon Storage in Alpine Grassland on the Qinghai Plateau. *PLoS ONE* **2016**, *11*, e0160420. [CrossRef]
158. Ni, J. Carbon Storage in Grasslands of China. *J. Arid Environ.* **2002**, *50*, 205–218. [CrossRef]
159. Fan, J.; Zhong, H.; Harris, W.; Yu, G.; Wang, S.; Hu, Z.; Yue, Y. Carbon Storage in the Grasslands of China Based on Field Measurements of Above-and below-Ground Biomass. *Clim. Change* **2008**, *86*, 375–396. [CrossRef]
160. Douglass, L.L.; Possingham, H.P.; Carwardine, J.; Klein, C.J.; Roxburgh, S.H.; Russell-Smith, J.; Wilson, K.A. The Effect of Carbon Credits on Savanna Land Management and Priorities for Biodiversity Conservation. *PLoS ONE* **2011**, *6*, e23843. [CrossRef]
161. Lyu, X.; Li, X.; Wang, K.; Zhang, C.; Dang, D.; Dou, H.; Lou, A. Strengthening Grassland Carbon Source and Sink Management to Enhance Its Contribution to Regional Carbon Neutrality. *Ecol. Indic.* **2023**, *152*, 110341. [CrossRef]
162. Zhang, J.; Brown, C.; Qiao, G.; Zhang, B. Effect of Eco-Compensation Schemes on Household Income Structures and Herder Satisfaction: Lessons from the Grassland Ecosystem Subsidy and Award Scheme in Inner Mongolia. *Ecol. Econ.* **2019**, *159*, 46–53. [CrossRef]
163. Ma, T.; Swallow, B.; Foggin, J.M.; Zhong, L.; Sang, W. Co-Management for Sustainable Development and Conservation in Sanjiangyuan National Park and the Surrounding Tibetan Nomadic Pastoralist Areas. *Humanit. Soc. Sci. Commun.* **2023**, *10*, 321. [CrossRef]
164. Wilkes, A.; Wang, S.; Lipper, L.; Chang, X. Market Costs and Financing Options for Grassland Carbon Sequestration: Empirical and Modelling Evidence from Qinghai, China. *Front. Environ. Sci.* **2021**, *9*, 657608. [CrossRef]
165. Sun, J.; Wang, Y.; Lee, T.M.; Nie, X.; Wang, T.; Liang, E.; Wang, Y.; Zhang, L.; Wang, J.; Piao, S.; et al. Nature-Based Solutions Can Help Restore Degraded Grasslands and Increase Carbon Sequestration in the Tibetan Plateau. *Commun. Earth Environ.* **2024**, *5*, 154. [CrossRef]
166. Zhao, X.; Xu, T.; Ellis, J.; He, F.; Hu, L.; Li, Q. Rewilding the Wildlife in Sangjiangyuan National Park, Qinghai-Tibetan Plateau. *Ecosyst. Health Sustain.* **2020**, *6*, 1776643. [CrossRef]
167. Dong, S.; Shang, Z.; Gao, J.; Boone, R.B. Enhancing Sustainability of Grassland Ecosystems through Ecological Restoration and Grazing Management in an Era of Climate Change on Qinghai-Tibetan Plateau. *Agric. Ecosyst. Environ.* **2020**, *287*, 106684. [CrossRef]
168. Mirchooli, F.; Kiani-Harchegani, M.; Khaledi Darvishan, A.; Falahatkar, S.; Sadeghi, S.H. Spatial Distribution Dependency of Soil Organic Carbon Content to Important Environmental Variables. *Ecol. Indic.* **2020**, *116*, 106473. [CrossRef]
169. Jin, Y.; Yang, X.; Qiu, J.; Li, J.; Gao, T.; Wu, Q.; Zhao, F.; Ma, H.; Yu, H.; Xu, B. Remote Sensing-Based Biomass Estimation and Its Spatio-Temporal Variations in Temperate Grassland, Northern China. *Remote Sens.* **2014**, *6*, 1496–1513. [CrossRef]
170. Huete, A.; Didan, K.; Miura, T.; Rodriguez, E.P.; Gao, X.; Ferreira, L.G. Overview of the Radiometric and Biophysical Performance of the MODIS Vegetation Indices. *Remote Sens. Environ.* **2002**, *83*, 195–213. [CrossRef]
171. Deering, D. Measuring Forage Production of Grazing Units from Landsat MSS Data. In Proceedings of the 10th International Symposium on Remote Sensing of Environment, Ann Arbor, MI, USA, 6–10 October 1975; ERIM: Ann Arbor, MI, USA, 1975; pp. 1169–1178.
172. Qi, J.; Chehbouni, A.; Huete, A.R.; Kerr, Y.H.; Sorooshian, S. A Modified Soil Adjusted Vegetation Index. *Remote Sens. Environ.* **1994**, *48*, 119–126. [CrossRef]
173. Jackson, R.D.; Huete, A.R. Interpreting Vegetation Indices. *Prev. Vet. Med.* **1991**, *11*, 185–200. [CrossRef]

174. Deng, Y.; Wu, C.; Li, M.; Chen, R. RNDSI: A Ratio Normalized Difference Soil Index for Remote Sensing of Urban/Suburban Environments. *Int. J. Appl. Earth Obs. Geoinf.* **2015**, *39*, 40–48. [CrossRef]
175. Liuzzo, L.; Puleo, V.; Nizza, S.; Freni, G. Parameterization of a Bayesian Normalized Difference Water Index for Surface Water Detection. *Geosciences* **2020**, *10*, 260. [CrossRef]
176. Gitelson, A.A.; Kaufman, Y.J.; Merzlyak, M.N. Use of a Green Channel in Remote Sensing of Global Vegetation from EOS-MODIS. *Remote Sens. Environ.* **1996**, *58*, 289–298. [CrossRef]
177. Steven, M.D. The Sensitivity of the OSAVI Vegetation Index to Observational Parameters. *Remote Sens. Environ.* **1998**, *63*, 49–60. [CrossRef]
178. Bou Kheir, R.; Greve, M.H.; Bøcher, P.K.; Greve, M.B.; Larsen, R.; McCloy, K. Predictive Mapping of Soil Organic Carbon in Wet Cultivated Lands Using Classification-Tree Based Models: The Case Study of Denmark. *J. Environ. Manag.* **2010**, *91*, 1150–1160. [CrossRef]
179. Huete, A.R. A Soil-Adjusted Vegetation Index (SAVI). *Remote Sens. Environ.* **1988**, *25*, 295–309. [CrossRef]
180. Marsett, R.C.; Qi, J.; Heilman, P.; Biedenbender, S.H.; Carolyn Watson, M.; Amer, S.; Weltz, M.; Goodrich, D.; Marsett, R. Remote Sensing for Grassland Management in the Arid Southwest. *Rangel. Ecol. Manag.* **2006**, *59*, 530–540. [CrossRef]
181. Jacques, D.C.; Kergoat, L.; Hiernaux, P.; Mougin, E.; Defourny, P. Monitoring Dry Vegetation Masses in Semi-Arid Areas with MODIS SWIR Bands. *Remote Sens. Environ.* **2014**, *153*, 40–49. [CrossRef]
182. Liang, T.; Yang, S.; Feng, Q.; Liu, B.; Zhang, R.; Huang, X.; Xie, H. Multi-Factor Modeling of above-Ground Biomass in Alpine Grassland: A Case Study in the Three-River Headwaters Region, China. *Remote Sens. Environ.* **2016**, *186*, 164–172. [CrossRef]

Disclaimer/Publisher's Note: The statements, opinions and data contained in all publications are solely those of the individual author(s) and contributor(s) and not of MDPI and/or the editor(s). MDPI and/or the editor(s) disclaim responsibility for any injury to people or property resulting from any ideas, methods, instructions or products referred to in the content.